UNIVERSITÀ DEGLI STUDI DI PADOVA

Dipartimento di Fisica e Astronomia "Galileo Galilei"

Corso di Laurea in Fisica

Tesi di Laurea

Studi sperimentali sulla luce diffusa per rilevatori di Onde Gravitazionali

Experimental investigations on light scattering for Gravitational Wave detectors

Relatore

Dott.ssa Livia Conti

Correlatore

Dr. Giulio Favaro

Laureando

Leonardo Dal Cin

Anno Accademico 2022/2023

Contents

Abstract

Negli interferometri laser per le onde gravitazionali, come ad esempio Advanced Virgo, una delle sorgenti residue di rumore tecnico è dovuto alla luce diffusa, che contribuisce a peggiorare la sensibilià dei rivelatori a basse frequenze. Luce diffusa può originarsi ad esempio quando i fasci laser interagiscono con elementi ottici, a causa della loro rugosità residua. Per questo motivo è importante caratterizzare le proprietà di diffusione della luce dei materiali e componenti utilizzati nel rivelatore. Il gruppo Virgo di Padova ha sviluppato un setup di misura del Bidirectional Scattering Distribution Function (BSDF) che descrive le proprietà diffusive in funzione nell'angolo di incidenza e di scattering. Il gruppo ha inoltre in dotazione una sfera integratrice che permette una misura integrale delle proprità di scattering, il Total Integrated Scattering (TIS). In questa tesi viene presentato il lavoro che ho svolto per migliorare il setup della misura di BSDF e le caratterizzazioni in termini di BSDF e TIS che ho fatto su diversi campioni di interesse per Virgo.

In the laser interferometers for gravitational waves, for example Advanced Virgo, one of the residual sources of technical noise is caused by the scattered light, that contributes to worsen the sensitivity of the detectors at low frequencies. Scattered light can originate, for example, when laser beams interact with optical elements, because of their residual roughness. For this reason it's important to characterize the light scattering properties of the materials and components used in the detector. The Virgo group of Padova has developed a setup for the measure of the Bidirectional Scattering Distribution Function (BSDF) that describes the diffusives properties as a function of incidence and scattering angles. Furthermore the group has an integrating sphere that permits an integral measure of the scattering properties, the Total Integrated Scattering (TIS). In this thesis is presented the work that I have done to improve the setup for the BSDF measure and the characterizations in terms of BSDF and TIS of various samples of interest for Virgo.

Chapter 1

Introduction

The Universe can be studied using signals of different nature. Historically light has played a primary role in this regard, but in recent time other messengers have become available. In particular major advances have been made possible by the recent detections of Gravitational Waves (GW), predicted theoretically by Albert Einstein in 1916 as a consequence of General Relativity (GR).
GW are a type of spacetime fluctuation whose effect is to change the relative distance between two free falling masses. They travel at the speed of light and carry energy and momentum. Here on Earth we can observe only the ones generated by very energetic astrophysical events. With ground based laser interferometers, e.g. Advanced Virgo [1] (Cascina, Italy) and Advanced LIGO [2] (Hanford and Livingston, USA), we can observe the final stages of coalescing binary neutron star (BNS), binary black hole (BBH) or mixed (NSBH) [3]. These instruments measures the difference in the amount of time required from light to travel in two arms of the interferometer, placed at 90°. In particular an initial laser beam, properly prepared, is split into two others by a beam splitter. These are then sent into two arms, before being reflected back and recombined at the beam splitter. The recombination is made so that there is destructive interference if the two arms have the same length. However the passage of a GW changes the arms length and a certain constructive interference can be measured.

Advanced LIGO and Advanced Virgo have observed so far 90 GW signals overall [4]. Among these it's worth mentioning at least **GW150914** and **GW170817** [5]. The first signal was observed by LIGO on the 14^{th} of September 2015. It's the first gravitational wave ever registered and confirms Einstein's predictions made a century before. This event is associated with the coalescence of two black holes of masses $35.6^{+4.7}_{-3.1}\,\mathrm{M}_\odot$ and $30.6^{+3.0}_{-4.4}\,\mathrm{M}_\odot$, distant 440 Mpc from us. **GW170817** was the first coalescence of two neutron stars recorded through gravitational waves (masses of $1.46^{+0.12}_{-0.10}\,\mathrm{M}_\odot$ and $1.27^{+0.09}_{-0.09}\,\mathrm{M}_\odot$, distant 40 Mpc from us). Less than two seconds after the GW signal, a short gamma-ray burst (GRB) was observed independently by the Fermi and Integral satellites. Because this allowed to gain a better understanding on the origin of short GRB, and because the event was also studied at different wavelengths thanks to the localization in the sky provided by LIGO-Virgo, this is considered the beginning of Multimessenger Astronomy with gravitational waves.
To observe GW with a certain frequency it's necessary to detect events that originates far from Earth. This implies that the usually registered waves are small (amplitude is inversely proportional from distance). Generally the ability to detect a relative length change $h \approx 10^{-21}$, or even less, is considered a requirement to be able to observe some signals per year. Given that $h = \Delta L/L$ and Virgo's arms are long $L = 3 \cdot 10^3$ m, a change of around $\Delta L \approx 10^{-18}$ m needs to be detectable in the best assumption. The detectors' sensitivity is usually expressed as maximum distance of a detectable *BNS* event: during the second observing run (O2), Virgo had a sensitivity of 28 Mpc, while at the end of O3 it was 61 Mpc [6]. Continue efforts are carried out to improve instruments performances and reduce the various noise sources. The most important ones, in the sense that are expected to be the major limits to the sensitivity, are summarized below and shown in figure 1.1 (left picture).

- Seismic noises. The overall movements of the ground cause oscillations in the instrument parts, particularly in the mirrors. This noise affects mainly the small frequencies and can be reduced

using systems of pendulums (*Superattenuators*) to support the mirrors.

- Thermal noise, caused by thermal oscillations in the detector's materials. It affects both the low frequencies (suspension thermal noise) and the central ones (coating thermal noise). Virgo works at room temperature, so one of the few ways to reduce this effect is to use specific and high quality materials.
- Quantum noise, associated with light's quantum nature. In particular it can be distinguished the *shot noise* that dominates the high frequencies and is caused by the photon single counting, and the *radiation pressure noise* important at low frequencies and caused by variations in the photons number that interacts with the mirrors.

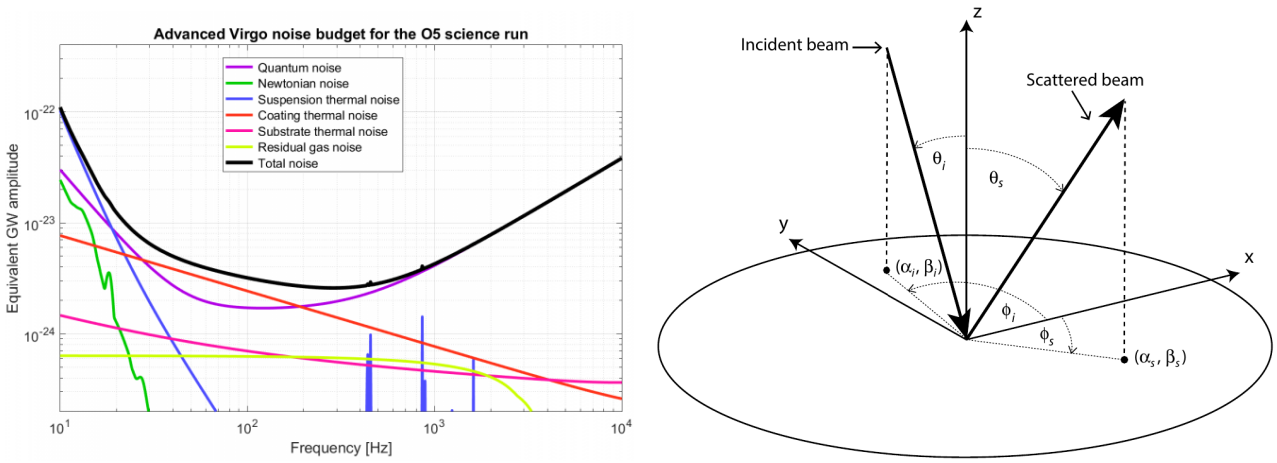

Figure 1.1: Left: Advanced Virgo noise budget for the O5 science run. Credit: [6]. Right: representation of the angles used in the BSDF definition in equation (1.2). Credit: [7].

There are also other "technical" noises caused by alignment controls, imperfect vacuum, actuators electronic noise, scattered light and others.
Scattered light is light that deviates from the beam trajectory. It can be problematic because movements of the surfaces where it's reflected can produce a phase noise if the light recouples with the main interferometer beam. The main sources of scattered light are: Rayleigh scattering caused by the air, surface dust contamination and residual roughness of the test masses and the optics. Mirrors and optics of high quality and that gives low light scattering can be used to mitigate the latter effect. The quantity that describes the scattering properties of a surface/object depending on the incident and scattered angles is the Bidirectional Scattering Distribution Function (BSDF). Often it's considered only the reflected part of the scattering (BRDF) or the transmitted one (BTDF). As expressed in [7], one can first define the radiance (L) as the radiant flux (or radiant power, Φ) emitted by a surface per unit of solid angle (Ω) and projected area $A\cos(\theta)$, and the irradiance (E) as the flux received per unit area:

$$L(\theta) = \frac{d^2\Phi}{dA\cos(\theta)d\Omega}; \qquad E = \frac{d\Phi}{dA} \tag{1.1}$$

The BSDF is defined as the radiance derived with respect to the irradiance:

$$BSDF(\theta_i, \phi_i, \theta_s, \phi_s) = \frac{dL(\theta_i, \phi_i, \theta_s, \phi_s)}{dE(\theta_i, \phi_i)} \ (\mathrm{sr}^{-1}) \tag{1.2}$$

where θ_i and ϕ_i are the elevation and azimuth angles of the incident beam, θ_s and ϕ_s alike but for the scattered beam. See figure 1.1 (right picture) for a visualization of these parameters. Another important quantity that characterizes the light scattering properties is the Total Integrated Scattering (TIS). It will be later presented in section 3.2.
This thesis work can be divided in two main parts. In the first one a setup for the BSDF measure, made by the Virgo Group of Padova, will be presented along with its characterization and improvements. In the second part the BSDF and TIS of three materials, relevant for the group, will be measured.

Chapter 2

Characterization and improvements of the BSDF measurement setup

2.1 Scatterometer description and BSDF computing

The scatterometer of the Virgo group of Padova is built to measure the samples BSDF on the incidence plane. Its optical layout is reported in figure 2.1. A continuous wave (CW) laser with a wavelength of 1064 nm and maximum power of 1 W is used as light source. The use of an half-wave plate ($\lambda/2$) and a polarizing beam splitter (BS) in front of the laser source, permits to obtain a linearly polarized beam whose power can be regulated by rotating the half-wave plate and using a dumper. Two mirrors direct the beam to the sample after passing through one (or two, see section 2.3) circular iris diaphragms. A second dumper is placed to block an eventual specular-reflected beam from the sample, while a third one is located behind it to block the transmitted beam. Behind the first mirror a photodiode measure the residual transmitted power and, using a calibration line, the incident power on the sample can be obtained. The laser and sample areas are separated by black cardboard panels to reduce possible interferences.
The sample is fixed using a semi-circular holder of radius ≈ 5 cm (see figure 2.5), made of aluminium and mounted on a rotating platform that can change the incidence angle θ_i (minimum rotation angle is 0.05 mm). The main detector is made by a circular photodiode of radius 0.5 mm attached to a rotating arm. It can be rotated 360° around the sample with a minimum step size of 0.5° and keeping the same distance from the center's rotation of 34.5 cm. An iris can also be mounted in front of the photodiode. Its aperture diameter is usually kept at 2 mm (see section 2.4).
The scattered power measured by the main detector is given as a voltage signal. To better isolate signal from noise, the laser is modulated with a square wave having frequency of 23 Hz. A lock-in filters the detector's signal by multiplying it with the modulation one and hence extracts the components at that frequency, which is then digitized and acquired by a computer. The system also measures the main detector's position using the angle $\theta = \theta_i + \theta_s$, starting from the incident beam direction.
For this setup the BSDF is obtained according to this formula:

$$BSDF = \frac{P_{det}}{P_{inc} \cdot \Omega \cdot \cos(\theta_s)} \tag{2.1}$$

where P_{det} is the power measured by the main detector, P_{in} is the incident power on the sample, $\Omega \approx 6.60 \cdot 10^{-6}$ sr is the solid angle in which the measured light is scattered into and θ_s is the scattered angle. The measured power can be obtained from the corresponding voltage using the following:

$$P_{det} = \frac{V_{LI} \cdot C \cdot F}{G \cdot R} \tag{2.2}$$

where V_{LI} is the voltage read by the lock-in, $C = 0.904$ is a conversion factor from the lock-in measured amplitude to the peak-to-peak amplitude, $G = 1.93 \cdot 10^{10}$ V/A is the photodiode gain factor, $R = 0.82$ A/W is the photodiode responsivity at 1064 nm and F is factor to consider the possible presence of neutral-density filters in front of the main detector.

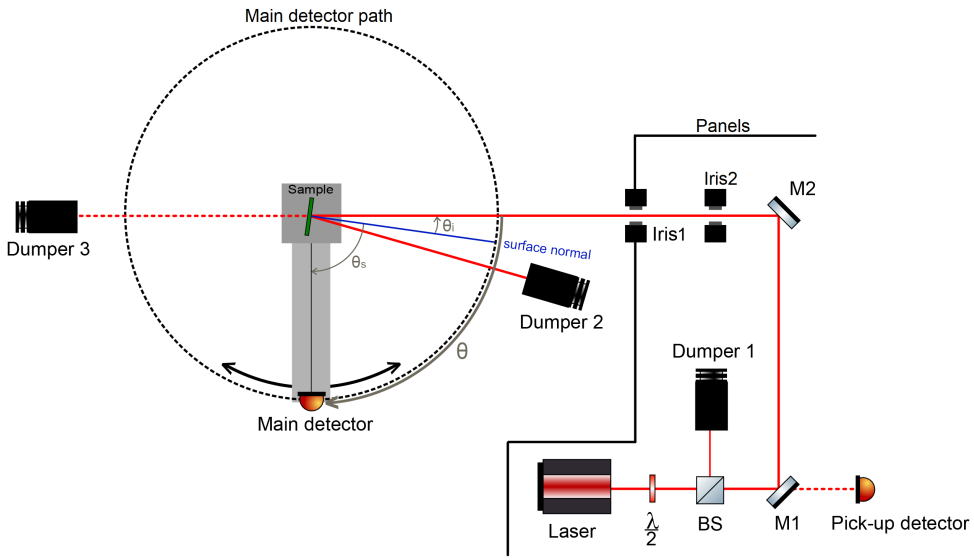

Figure 2.1: Optical layout of the scatterometer. Image credit: Izumi Schmiegelow.

2.2 Tube and irises effects

The first procedure that I did on the scatterometer was a realignment of all its parts. This was done by first correcting the vertical placement of the different components to be at beam's height (around 18 cm). The mirrors positions and orientations were set in order to have the beam centered on the sample holder and on the dumper at the end. It's important to always check if this last condition is satisfied because even a small change in the dumper alignment can drastically increase the signal level. An example of this effect can be seen in figure 2.2. In there are reported three sets of voltage measure, i.e. the signal measured by the main detector, with beam power of 1 W, no sample, and with all the irises on the main beam path opened. Also on *dumper 3* an opaque-black tube can be mounted to better capture the residual beam and avoid further reflections that can increase background level, see figure 2.4.

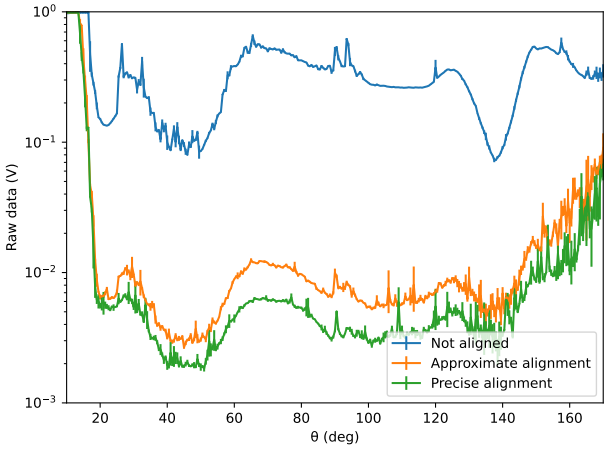

Figure 2.2: Effects of end dumper alignment on the background measures. The three sets of measures were taken in the same conditions, only the end dumper alignment was changed.

Iris diaphragms can be placed on the beam path to reduce possible stray reflections from the laser source area. The used beam has approximately a Gaussian profile so, like reported in [8], its intensity is described by the function:

$$I(r,z) = \frac{2P}{\pi w(z)^2} e^{-2\frac{r^2}{w(z)^2}} \tag{2.3}$$

where P is the power, $\omega(z)$ the beam radius and r the distance on the plane normal to the propagation direction z. For this reason a significant part of the power may be lost on the passage through an iris, depending on its aperture.

The mirrors used in the setup have a power loss of around 3 ppm, so for our purposes a power loss of 1 ppm is considered acceptable. A displacement of the beam with respect to the iris center is also possible: based on how precise the latter can be manually moved, in the wort case scenario the displacement is estimated to be 1.5 times the beam's radius ($w(z) \approx 0.5$ mm, estimated from previous measures on the setup). Following the work in [8], the minimum iris acceptable aperture radius is around 2 mm, as can be seen by figure 2.3.

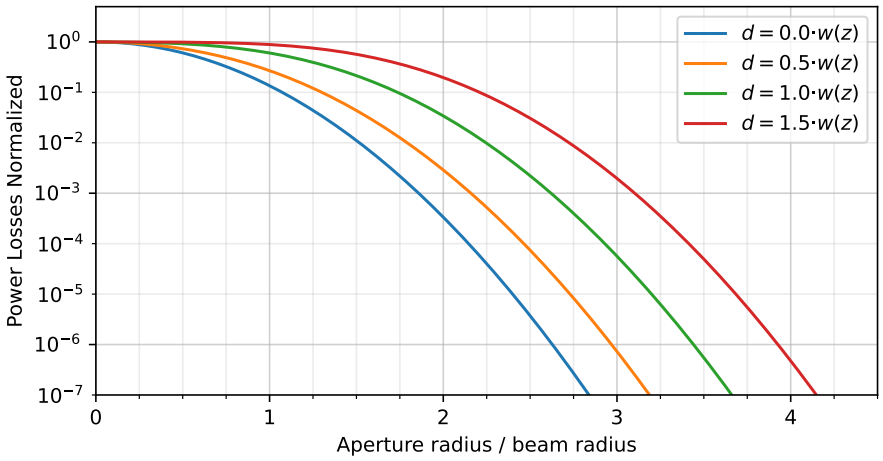

Figure 2.3: Power loss for a Gaussian beam through a circular aperture with a lateral displacement d and beam' radius $w(z)$. Credit: [8]. If the maximum normalized power loss that is acceptable is 10^{-6}, $w(z) \approx 0.5\,\text{mm}$ and $d = 1.5 \cdot w(z)$, then the minimum value for "Aperture radius/beam radius" is 4. This corresponds to an iris radius of $\approx 2\,\text{mm}$.

Some measures with the scatterometer were taken to test the irises effect on the background signal. Since these weren't graduated, their radius measures are approximate. In particular the following aperture were tested: open (radius $\sim$ 12 mm), half open (labelled "1/2", radius $\sim$ 6 mm), a third open (labelled "1/3", radius $\sim$ 4 mm). Note that these values are larger than the worst-case scenario mentioned before, so the power loss can be considered negligible.
For starter only a single iris, labelled "*iris1*" (see scatterometer layout in figure 2.1) was taken into consideration. The tests were conducted by measuring the background signal given by the laser beam with power of 1 W, without the sample holder, and the results are reported in figure 2.4. Note that the peak seen around $\theta = 90°$ is caused by the way in which the BSDF is computed from the raw data (eq. 2.1), in particular from the term $1/\cos(\theta)$ (since $\theta_i = 0$, then $\theta = \theta_s$).

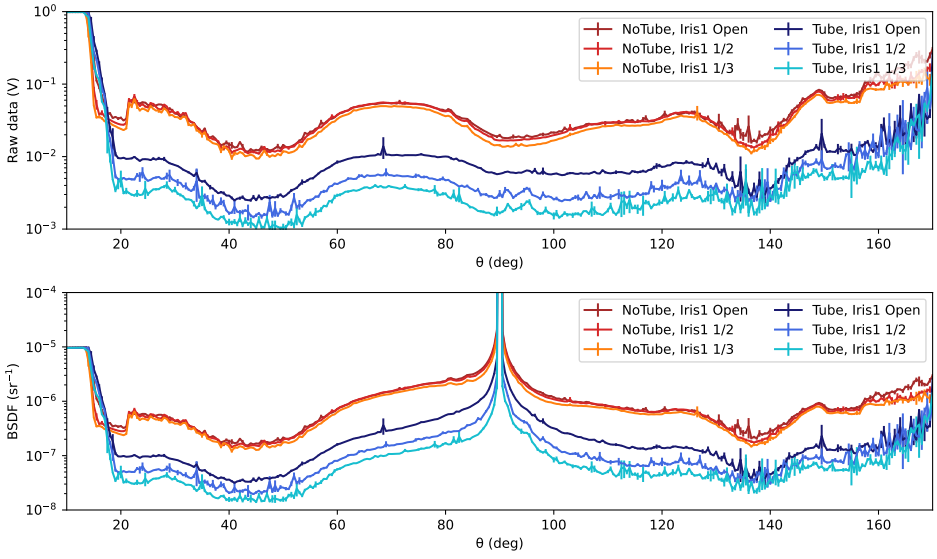

Figure 2.4: Background measurements with and without the tube on *dumper 3*, changing iris1 aperture. The region considered is between $\theta = 10°$ and 170°, with a step size of 0.5°. It can be seen the reduction in the general background level caused by the tube. Also iris1 can be used to further reduce this value, improving the sensitivity. In $\theta = 90°$, for the BSDF data, a peak can be seen. It is caused by the way in which the BSDF itself is obtained, in particular from the term $1/\cos(\theta)$ in eq. (2.1). See figure 2.1 for the angle θ is considered.

The background is reduced at most angles thanks to the tube presence on the end dumper. Furthermore, in this condition, the improvement caused by the iris becomes relevant. The best configuration

found is with *iris1* open to a third (*iris1 1/3*), in agreement with a greater reduction of stray beams. Smaller apertures aren't advised with the current setup. In fact with the detector positioned at 180° from the incident beam direction, the given signal starts to decrease significantly when the aperture radius is between 2 and 3 mm, depending on how well the optics are aligned. In this regard an aperture of 4 mm is a good compromise and it will be used as standard working condition for future measures.

Similarly the iris effect on the background was also studied with the sample holder mounted. This is composed of a semi-circular frame on which there can be mounted arms to fix samples at most 2 mm thick using screws, see figure 2.5. Both the frame and the arms are made of aluminium. In section 2.3 it will be shown how the arms presence gives a major contribution to the background level. To reduce this effect a second iris, labelled "iris2", was placed in between "iris1" and the second mirror, see figure 2.1, at around 5 cm from the former.
Initially, a preliminary set of measures was taken to test the new component impact on the background. These were acquired without the holder's frame and with *iris1* in the best configuration found before. The results are reported in figure 2.6.

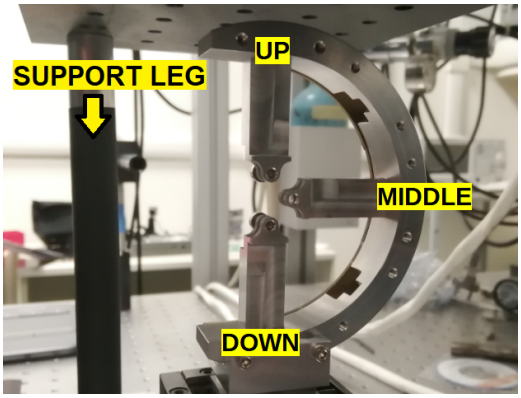

Figure 2.5: Semicircular frame, arms and their main positions labelling on the sample holder. A support leg of the apparatus can be seen on the left.

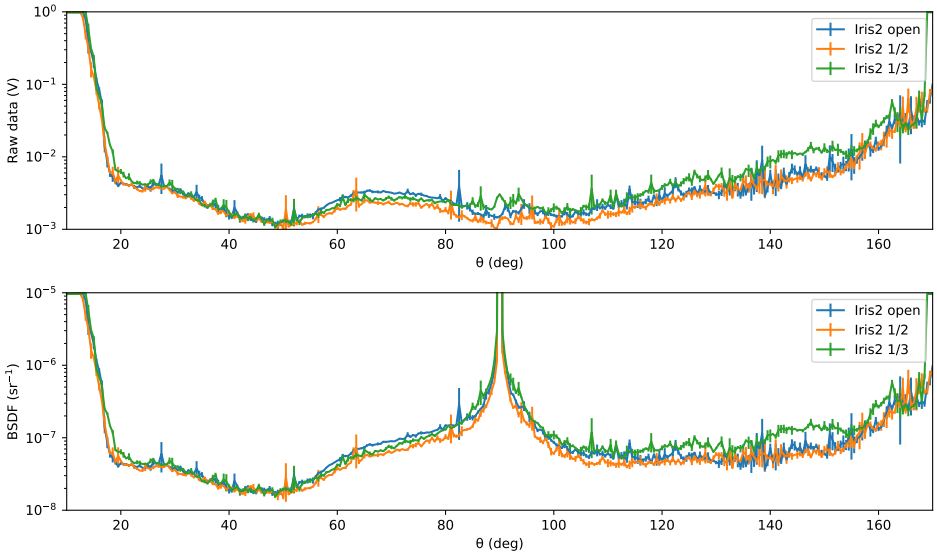

Figure 2.6: Background taken with a beam power of 1 W, the tube mounted on *dumper 3*, *iris1* open of 1/3 and changing *iris2* aperture. In can be seen how, in these conditions, the effect of *iris2* seems to be negligible. The peak at $\theta = 90°$ is caused by the way in which the BSDF is computed, in particular from the term $1/\cos(\theta_s)$ in equation 2.1. In this case $\theta_i = 0$, so $\theta = \theta_s$.

"Iris2" has a small impact on the background, so its use doesn't invalidate the conclusions made so far. Also, changing its aperture, a significant variation in the signal trend wasn't seen, save from the region around $\theta = 150°$. The slightly higher signal for "*iris2 1/3*" may be caused by stray reflections from misaligned irises. Their positioning was improved in the following measures, so this effect isn't concerning.
Figure 2.7 shows various measures taken with just the holder frame mounted, and in the same conditions as before. It can be seen that the "Iris1 1/3, Iris2 open" and "Iris1 1/3, Iris2 1/3" are very similar to each other. It would seem that also in these conditions *iris2* has a negligible effect. Despite this in section 2.3 it will be shown how the latter can be used to reduce the background when also the sample holder's arms, and not just the frame, are mounted on the setup.

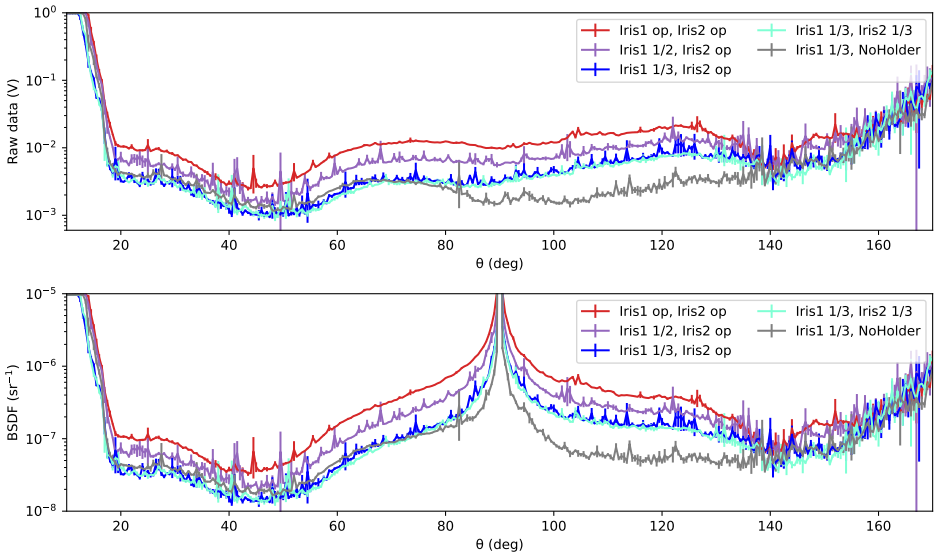

Figure 2.7: Background measures taken with a beam power of 1 W, the tube mounted on *dumper 3* and changing the aperture of *iris1* and *iris2*. The sample holder frame was mounted for all the measure, except for "Iris 1/3, NoHolder" which is reported just as a comparison. From these data it can be seen that, on the background given by the sample holder frame, *iris2* has a negligible effect.

2.3 Sample holder and arms effects

The sample holder arms can be mounted in different positions and numbers to better adapt at the possible samples shapes. Usually only two arms are employed. The most used positions are shown in figure 2.5. To test their effect on the background a set of measures changing both *iris1* and *iris2* apertures is reported in figure 2.8. The arms are in the up-down positions at a distance of 15 mm from each other, measured from their tip, and the beam passes in the middle between the two.

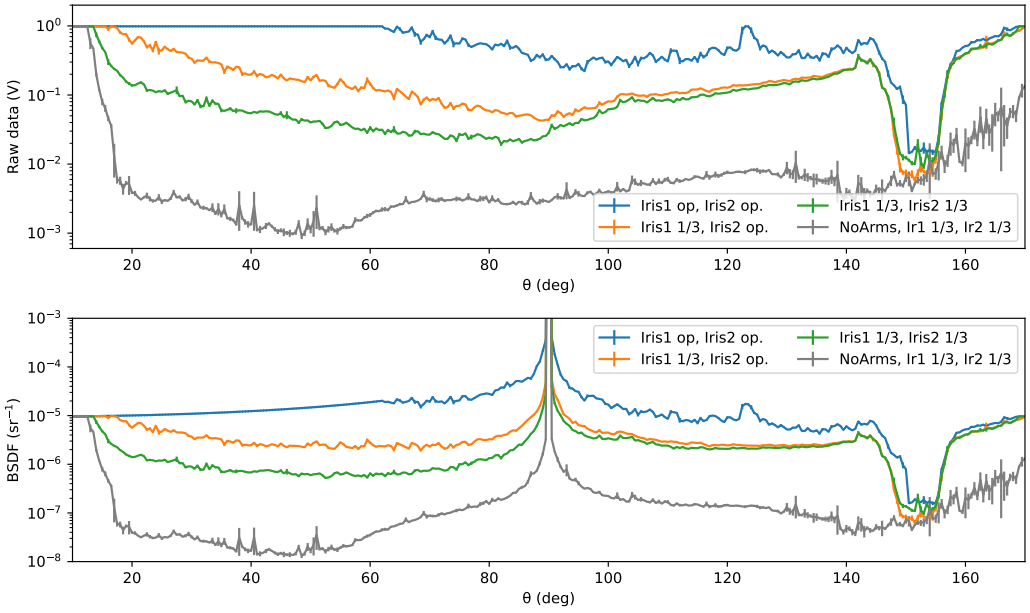

Figure 2.8: Background measures with holder and 2 arms mounted (up-down position). Arms distance from the lower edges = 15 mm. In the first measure, "Iris1 op, Iris2 op", the signal is saturated up to $\theta \sim 60°$. Regardless it can be seen the background reduction caused by *iris1* and *iris2*, especially in the reflection part for the latter. A sharp signal decrease in the region around $\theta = 150°$ can also be seen. It is caused by the presence of a support leg of the apparatus, see figure 2.5, that cast shadow over the main detector: this drop has no physical significance and those data should not be considered.

Note that in figure 2.8, the measure with all the irises open isn't ideal because, up to $\theta \sim 60°$, the signal is saturated. The improvement caused by the irises, however, can still be seen especially at angles lower than 90° for *iris2*. For this reason, in all the BSDF measures reported in the following work, the configuration with *iris1* and *iris2* opened at a third (radius $\approx 4\,\text{mm}$) will be considered a standard working condition, even when not specified.

Regardless, the difference with the signal obtained without arms is important. A possible explanation could be found in the beam Gaussian nature. Beam's power relatively distant from it's center may be scattered by the arms surfaces and increase the overall background. To test this hypothesis a simulation can be made. The arms can be modeled as two annulus sector where the opening angle is θ_b, the larger radius is ∞ and the smaller one is R, (see figure 2.9 right). Considering a Gaussian beam with power P_0 and beam radius w, the power seen by the front surface of the two arms (P_{inc}) is given by the surface integral of equation (2.3):

$$P_{inc} = \int_{\Sigma_{arms}} I(r)\, d\Sigma = \int_0^{2\theta_b} d\theta \int_R^{\infty} I(r) r\, dr = \frac{P_0 \theta_b}{\pi} \cdot e^{-\frac{2R^2}{w^2}} \tag{2.4}$$

To ease the computation, and for a rough understanding, it may be assumed that all the light fraction seen by the arms front surfaces is scattered uniformly over the projected solid angle of a sphere. The assumption was not limited only to the reflection hemisphere because, as can be seen for example in figure 2.8, the arms presence has an effect even in the "transmission part" of the graph, i.e. for $\theta > 90°$. Also the irises effect can be ignored because a worst-case scenario is being considered.
In these assumptions the scattered power that is measured by the detector is:

$$P_{measured} = P_{inc} \cdot \Omega/(4\pi) \tag{2.5}$$

where $\Omega \approx 6.60 \cdot 10^{-6}\,\text{sr}$ is the solid angle in which the measured light is scattered into and 4π is a sphere's solid angle. From this, equation (2.1) can be used to compute the arms BSDF contribution. A baseline value of $BSDF_{base} = 1 \cdot 10^{-8}\ \text{sr}^{-1}$ was also added to this contribution to approximate the lower background signal seen without arms in figure 2.7.

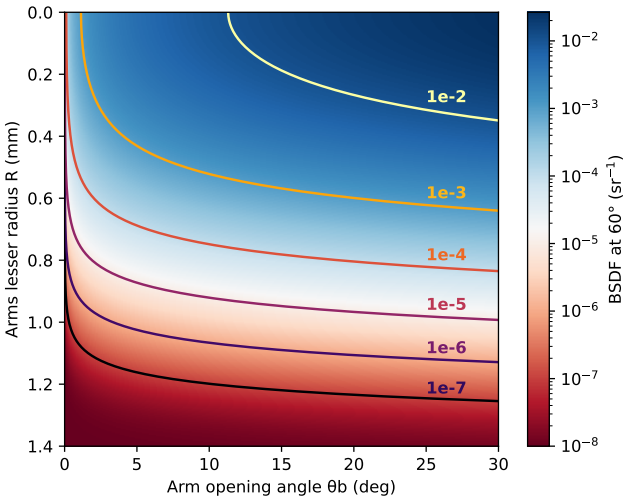

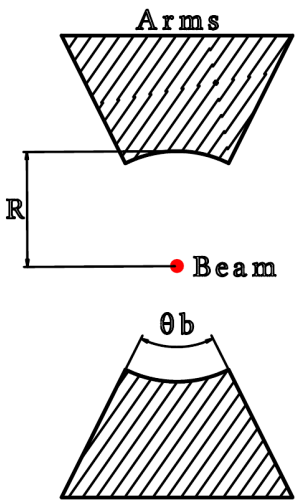

Figure 2.9: Left: simulated BSDF contribution from the modeled arm's scattered light at $\theta = 60°$, changing the arms parameters, plus a baseline of $1 \cdot 10^{-8}\ \text{sr}^{-1}$. A Gaussian beam with power $P_0 = 1\,\text{W}$ and beam radius $w = 0.5\,\text{mm}$ was considered. Right: Arms shape used in the simulation, modeled as two annulus sector, as viewed from the beam's direction. θ_b is the opening angle and R the lesser radius. The greater radius is considered ∞.

Figure 2.9 (left) shows the simulated BSDF results for the angle $\theta = 60°$. Note that the BSDF value strongly depends from the arms distance, i.e. the double of "arms lesser radius R", while the opening

angle θ_b is less important. The BSDF also drops rapidly to the baseline level for relatively small arms radius ($R \approx 1.4\,\text{mm}$).

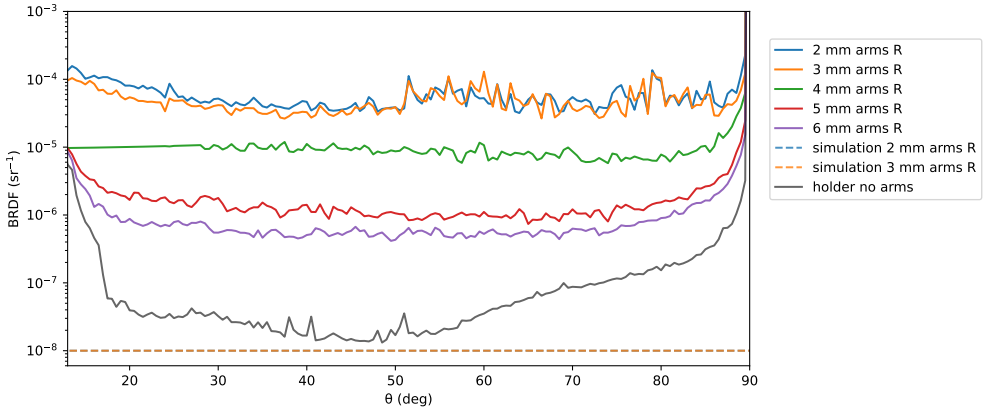

Figure 2.10: Experimental and simulated background with two arms (up-down position) changing arms distance and with the laser beam passing in the middle between the two. For the simulated data it was considered a beam with power $P_0 = 1\,\text{W}$ and beam radius $w = 0.5\,\text{mm}$. For the arms model it was considered $R =$ (arms distance)/2 and $\theta_b \sim 28°$. The simulated scattered power from the arms is so low that the only significant contribution is given by $BSDF_{base} = 1 \cdot 10^{-8}\ \text{sr}^{-1}$, like expected from what was already seen in figure 2.9 (left).

Figure 2.10 shows a comparison between measured and simulated BSDF from the arms scattering. For the latter, the BSDF contribution given by the power expressed in equation (2.5) is so low that essentially only the baseline $BSDF_{base} = 1 \cdot 10^{-8}\ \text{sr}^{-1}$ is relevant, in agreement with figure 2.9. Therefore the Gaussian nature of the beam seems to not be the cause of the relative high scattering from the arms seen in figure 2.8. It's suspected that there is a non-Gaussian contribution that interferes with the arms. From the measure in figure 2.11 it was also found that when one arm is mounted in the "*middle*" position (as in figure 2.5) the background is generally up to almost one order of magnitude higher than the background given by an arm in the "*up*" or "*down*" position.

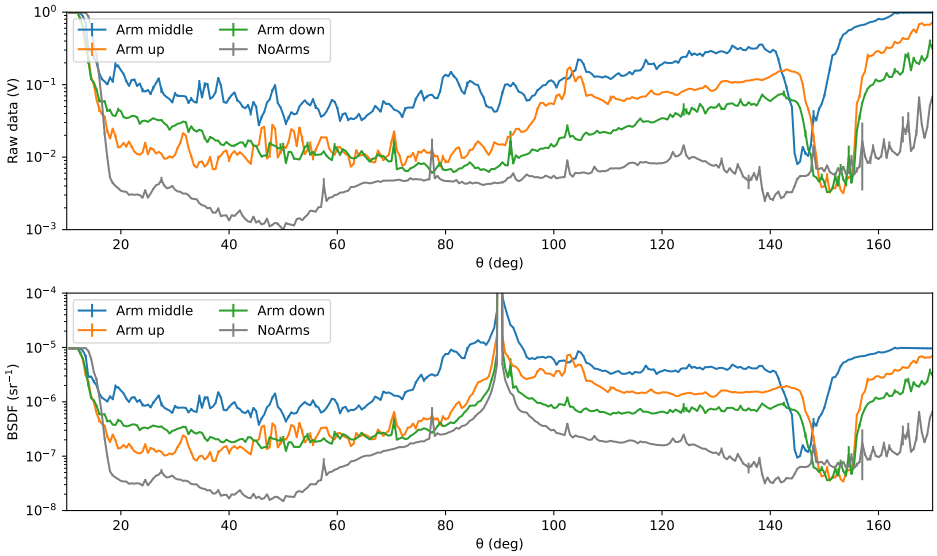

Figure 2.11: Background measures with one arm in different positions on the sample holder, beam power 1 W, irises in the best configuration found at the beginning of this section. For all positions the distance between the arm tip and the beam is $R \approx 6\,\text{mm}$. It can be seen that the "middle" position generally gives a higher signal than the "up" or "down". Also the region around $\theta = 150°$, where the shadow cast by a support leg of the apparatus can usually be seen, is slightly different for the arms in the "middle" position.

Further investigations are needed to better characterize the origin of this effect. Regardless, to reduce

the background, some improvements could be made in the arms design, for example: employing thinner ones to decrease the surface exposed to light or coat them with light absorbing paint to further limit the amount of scattered light.

2.4 Detector's view angle

As stated in section 2.1, in front of the main detector there is an iris to regulate the amount of light arriving at the photodiode. Having a correct aperture for this iris is important to reduce the unwanted signals read by the detector. For all the BSDF measures taken in previous sections and the ones that will be presented in chapter 3, this iris was kept open with a diameter of 2 mm. This value was established using the following procedure. First a stack of neutral-density filters (overall power reduction of around $\approx 8 \times 10^6$ times) was mounted on the detector to avoid damaging the main photodiode and the latter was placed in the position corresponding to $\theta = 180°$ (main detector directly on the beam path). Then, in order to not saturate the detector, the beam power was further reduced by operating the half-wave plate. Finally the detector's iris aperture was reduced until a significant decrease on the signal, read with an oscilloscope, was observed. In this condition the final value of the iris diameter is ~ 2 mm.
The main detector iris can be used to change the photodiode field of view, thereby determining the amount of light power (P) measured by it. Having d as the iris diameter it can be assumed as a first approximation that this power follows a quadratic law: $P = c + bd + ad^2$. Three main contributions can be seen depending on the diameter: a constant one "c" (e.g., electric noise, because it depends just from the electronics), a linear one "bd" (e.g., scattered power directly from the beam, located on the horizontal plane where the measuring photodiode and the beam are positioned. This contribution depends from how much of the plane "is seen" by the photodiode and thus from the iris aperture diameter) and a quadratic one "ad^2" (other light which don't directly comes from the scattered light on the horizontal plane, so their contribution depends from the surface of the iris aperture rather than just the diameter). Detector's filed of view should be such that the linear contribution, i.e. the power scattered directly from the beam on the horizontal plane which we want to measure with the current setup, is greater than the other sources. Since the constant contribution depends from certain factors that cannot be easily changed, like the electronics, the comparison should be made between the linear and the quadratic contribution. To establish these, background measurements were taken every 10°, between 20° and 160°, changing the iris diameter of 0.5 mm from 1 mm to 5.5 mm. The data were taken with the sample holder frame mounted, without holder's arms and with a beam power of ≈ 1 W.

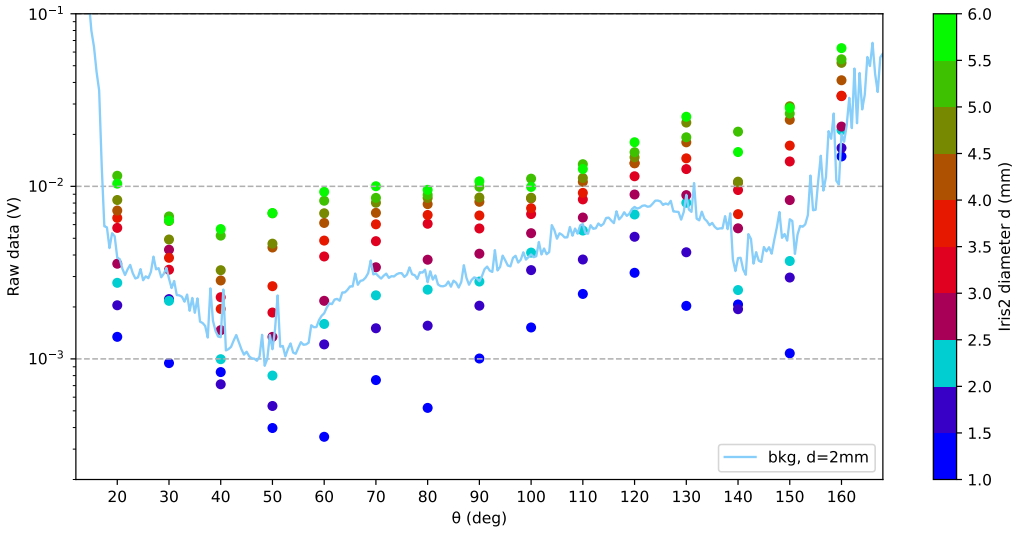

Figure 2.12: Background raw signal (voltage) changing the main detector's iris aperture. Beam power ≈ 1 W. The measures were taken with the sample holder frame mounted, but without arms. Each shown point is the average value of three repeated measures, taken in the same working conditions. A typical background measure with the iris having a diameter $d = 2$ mm is also reported as a continuous line.

Figure 2.12 shows the raw data obtained and compares them with a typical background. Each shown point is actually the average value of three repeated measures taken in the same conditions.
The voltage data were converted in power using equation (2.2). From a preliminary series of quadratic fits, with all parameters bounded to be non-negative in order to have physical meaning, it was found that the constant contribution "c" was compatible with zero for almost all angles. So the fits were repeated without considering c ($c = 0$). The errors on the power values were considered as the standard deviation of the three repeated measures.
In the interest of clarity, in figure 2.13 is shown only one of the final fits as an example, in particular the angle $\theta = 60°$. The reduced $\chi^{(2)}$ ($\chi^{(2)}_{red}$) for each angle are reported in the table on the side. Their values seems to change randomly depending on the angle, but they generally tend to be $\chi^{(2)}_{red} > 1$, which could mean that the considered power errors underestimate the real ones. The other parameters obtained from the fits, i.e. a and b, will be represented as the corresponding power contributions in figure 2.14.

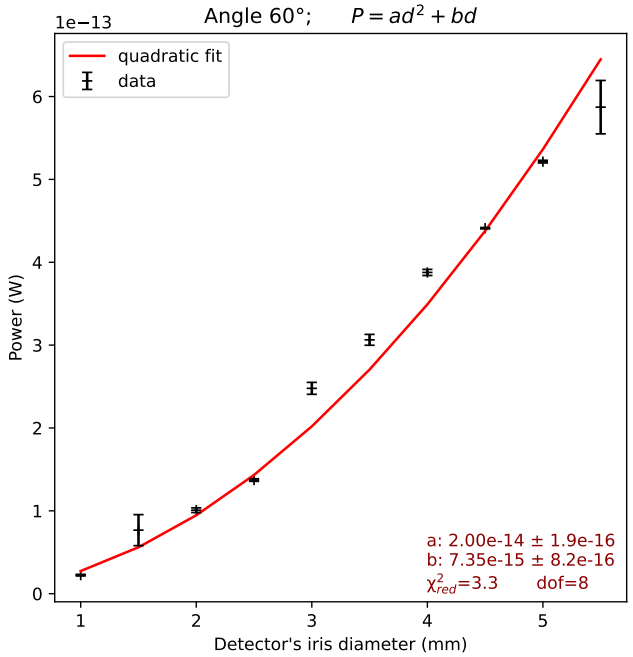

Angle (°)	$\chi^{(2)}_{red}$
20	0.21
30	5.1
40	3.1
50	3.8
60	3.3
70	32
80	39
90	14
100	99
110	0.18
120	0.34
130	9.4
140	6.2
150	1.3
160	0.44

Figure 2.13: Left: example of scattered power changing the main detector's iris diameter for the angle $\theta = 60°$. The quadratic fit ($P = ad^2 + bd$) with non-negative bounded parameters is also reported. Right: reduced $\chi^{(2)}$ values ($\chi^{(2)}_{red}$) for the quadratic fits ($P = ad^2 + bd$) of all angles.

Despite this results some interesting considerations can be made on the linear (bd) and quadratic (ad^2) power contributions. These are reported in figure 2.14 for each angle: the parameters values a and b were obtained from the previously described quadratic fits, while the iris diameter was considered $d = 2\,\text{mm}$. It can be seen that the linear contribution trend (bd) is qualitatively similar to the usual background measures, for example the one reported in figure 2.12. In fact for $\theta \leq 90°$ "bd" values are generally smaller than the ones found for $100° \leq \theta \leq 130°$; there is a drop around $\theta = 150°$ and then the value rises again. Near 50° "bd" goes to zero and this corresponds to the signal's minimum seen in figure 2.12. Around 150° a similar behavior is present but this may be liked to the fact that a support of the scatterometer's apparatus casts a shadow over the main detector (see figure 2.11 for an example of this effect) and so it's reasonable for "bd" to tend to zero because no direct scattering from the beam can be observed.
The quadratic contribution "ad^2" tends to remain relatively small compared to "bd", except between 40° and 60°, and around 150°. For the latter this can be explained again by the support's shadow that suppresses the linear contribution.
Considering all this, it can be said that for a main detector's iris opened with diameter $d = 2\,\text{mm}$ the main contribution to the power depends *linearly* from the diameter of the iris itself, at least for most

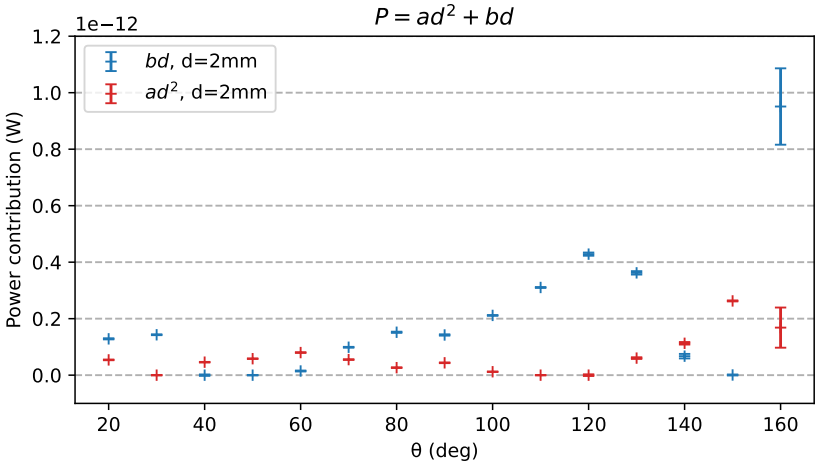

Figure 2.14: Estimates of the observed power contribution with an iris on the detector opened with a diameter d=2 mm. The values for a and b were obtained from the quadratic fits ($P = ad^2 + bd$) of the power data introduced in this section.

angles. Therefore the aperture found with the procedure set out at the beginning of this section seems to effectively put the setup in a good configuration, in which the main part of the received power is caused by the beam scattering on the horizontal plane and not from unwanted sources. A way improve the completeness of the analysis would be, for example, to check if the behavior observed here still holds true if a sample is placed on the holder.

Chapter 3

Sample characterization

The setup for measuring the BSDF, characterized and improved as detailed in the previous chapter, is used by the Virgo and ET Padova groups to investigate materials and coatings of interest for GW detectors. In this thesis I have worked at the characterization of silicon wafers, anodized aluminum and a plastic material.
Silicon wafers can be used, for example, as surfaces to collect dust particulates that may be present in various environments of the Virgo interferometer. From the amount of dust deposited in a certain time there can be obtained an estimation of the dust that may deposit on the Virgo optics and from there one can estimate the contributed stray light [9]. The anodized aluminium and plastic material analyzed will be used in a new installation of the scatterometer, so it's useful to know their properties.

3.1 BSDF measures

For these measures the main scatterometer's irises were kept opened with a radius of 4 mm, as expressed in section 2.3. In addition to the details described in the previous chapter, some extra care is needed when measuring samples. They must be placed such that incident beam angle (θ_i) is non-zero, in particular it was chosen to keep it at $\theta_i = 6.5°$. This is to stop the specular reflected beam with a dumper and prevent it to enter the laser source zone, causing possible disturbances or damages to the source itself. As seen in the optical layout 2.1, *dumper 2* is used to block this beam and minimize its contribution to the detector's observed power.
To better compare the backgrounds of the various materials they have been modeled using the function (3.1), where the term $1/\cos(\theta - \theta_i)$ is used to reproduce the same singularity effect caused by the way in which the BSDF is computed (eq. 2.1). For simplicity only the reflection part ($\theta < 90° + \theta_i$) will be considered in the fits.

$$BSDF_{bkg}(\theta = \theta_i + \theta_s) = \frac{a\theta^2 + b\theta + c}{\cos(\theta - \theta_i)} = \frac{a\theta^2 + b\theta + c}{\cos(\theta_s)} \tag{3.1}$$

It's possible for the scattered power to saturate the photodiode's signal. To avoid this, laser's power can be reduced by operating the half-wave plate, or mounting neutral-density filter (ND filter) in front of the main detector. The power reduction of the used ones is reported in table 3.1.

Filter ND	P_{in}/P_{out}
1.3	14
3	92

Table 3.1: Power reduction (P_{in}/P_{out}) of the neutral-density filters used in the BSDF measures.

These corrections are included in the BSDF computing in equations (2.2) and (2.1), but not in the raw data which cannot then be directly compared as referring to different impinging power levels.

3.1.1 Silicon DSP

Silicon wafers, depending on the number of polished surfaces, can usually be distinguished between Single Side Polished (SSP) or Double Side Polished (DSP). For the purposes of this thesis only the latter type will be considered. In particular the sample that was analyzed is a quarter of a circle of radius $\approx 2\,\text{cm}$ and thick $\approx 0.5\,\text{mm}$, as represented in figure 3.1.

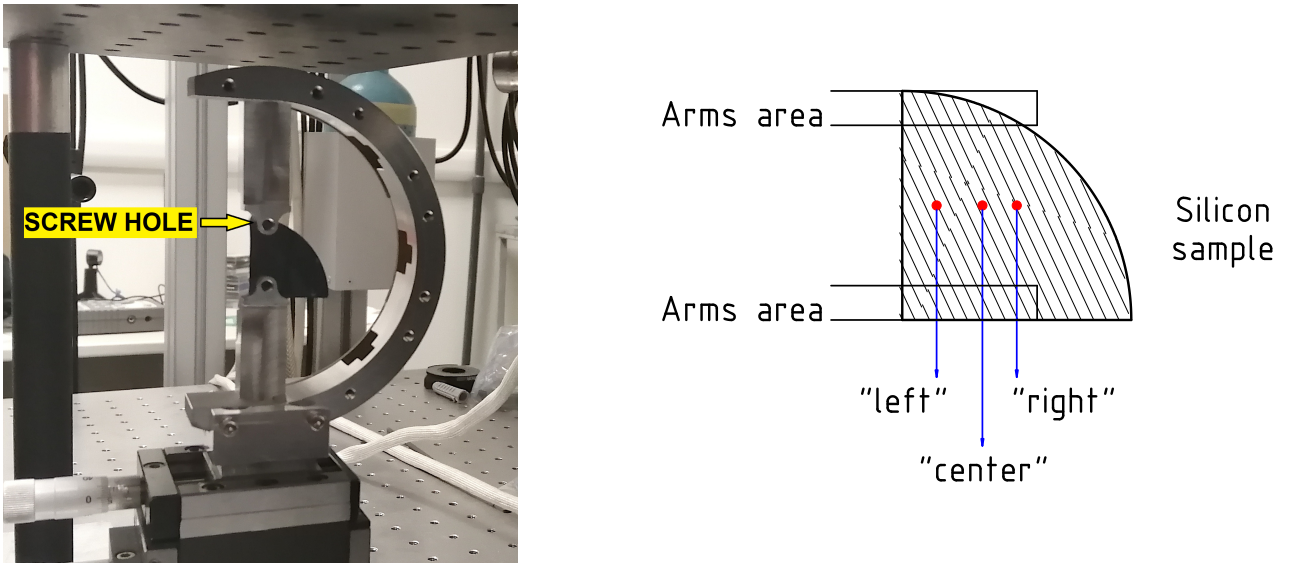

Figure 3.1: Left: silicon DSP mounted on the sample holder. It's also pointed out the screw holes position used to fix the sample in place. Right: sketch of the silicon DSP sample, area occupied by the holder's arms and label of the measured points (*right*).

The wafer was mounted on the sample holder using two arms in the *up* and *down* positions, distant around 14 mm from each other, and fixed using two screws in the holes visible in figure 3.1 (left). A power meter and the scatterometer's 1064 nm laser, with a power of 500 mW, were used to obtain an estimate of the sample's reflectance (R) and transmittance (T). It was found out that $R \sim 0.45$ and $T \sim 0.36$.
For the BSDF measures, three different spots on the sample, distant around 5 mm from one another, were considered. They are represented in figure 3.1 (right). The spots were changed by just loosening the screws and shifting the sample so that the background caused by the sample holder and the arms would remain the same. The measuring procedure used is similar to the one employed for the background and detailed in section 2.2. The results are reported in figure 3.2. For the sample's measures a filter *ND3* was used to not saturate the detector (table 3.1). The background, taken in the sample absence, was instead measured without the filter because a reduction of about 2 orders of magnitude would have made it almost indistinguishable from the electrical noise. The model parameters, found by fitting the respective data with eq. (3.1), are reported in the first column of table 3.2.
The measure labelled "*dark*" was taken without the sample and with the laser turned off. It's essentially the signal given by the electrical noise and the lower limit for the electronics sensitivity. In the region around $\theta = 150°$ it's expected to detect only the electrical noise because the beam's view is blocked by a leg of the system that supports the setup (see figure 2.5).

Figure 3.2 shows a certain variability in the BSDF depending from the measured location. To test if these could be explained by random variations of the signal, two distinct series of data were taken with the laser pointed on the same sample spot and the results are reported in figure 3.3.

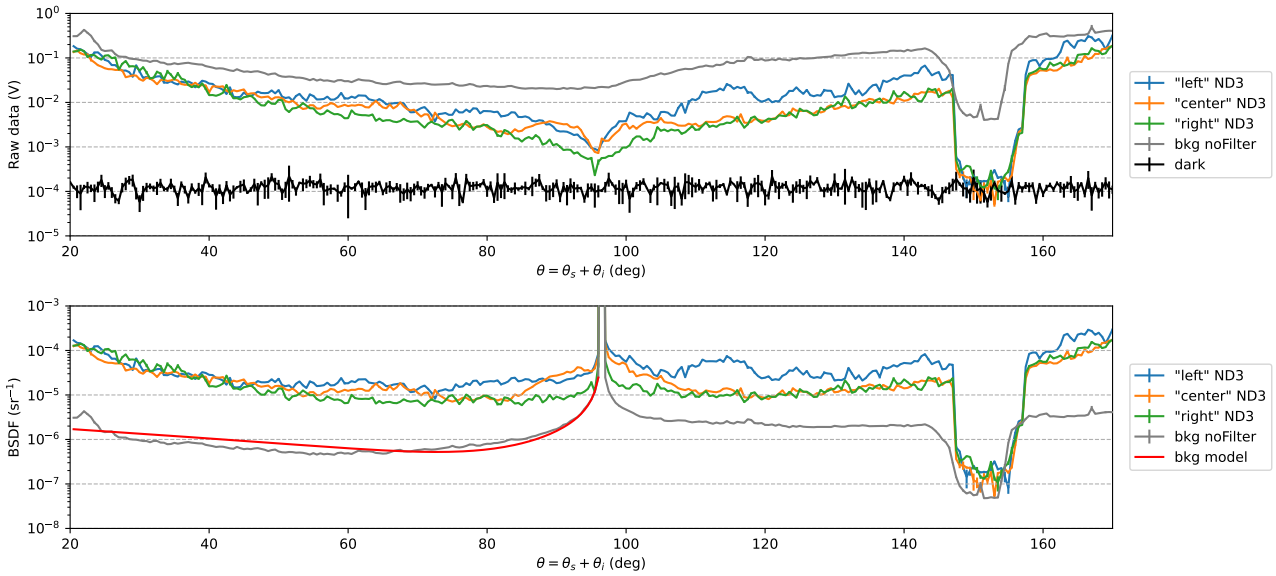

Figure 3.2: Measures of BSDF for silicon DSP, considering both the reflection and transmission. Laser power $\sim 1\,\mathrm{W}$, incident angle $\theta_i = 6.5°$. All measures were taken using a filter *ND3* to not saturate the detector, except the background and the dark. At $\theta = \theta_i + \theta_s = 96.5°$ the singularity caused by the factor $1/\cos(\theta_s)$ on the BSDF computation (2.1) can be seen.

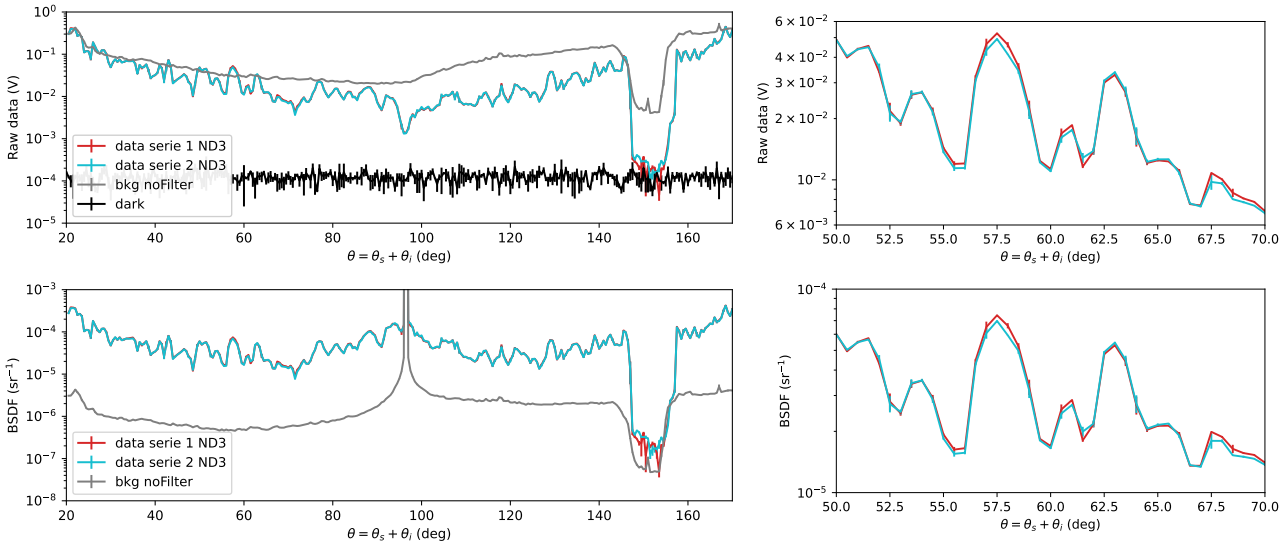

Figure 3.3: Left: two repeated measure on the same sample's spot for the silicon DSP. Also the background and the dark signal (electrical noise) is reported. The data series were taken using a filter *ND3* to not saturate the detector, while the background was taken without filters. This is why, for the raw data, the latter appears to be higher than the silicon's measure. Right: zoom on the region 60°-80°. It can be seen how the two data series shows negligible differences despite being taken in different moments. Laser power $\approx 1\mathrm{W}$, incident angle $\theta_i = 6.5°$.

At least from a qualitative comparison, the differences between the two series are around an order of magnitude, or more, smaller than the ones seen in figure 3.2 by changing the sample's position. Therefore it can be assumed that the variability in 3.2 is caused by effects linked to the particular surface of the sample and not by a random variation of the signal. In this regard it may be worth mentioning that the silicon sample had been in use for some time before the measures and no particular cleaning operation was done on it. For this reason a possible downgrade of the analyzed surface quality (e.g., micro-scratches) or the presence of dust particles could have had an impact on this variability.

3.1.2 Plastic

The plastic material analyzed is the one chosen for the new installation of the scatterometer in a clean room. It will be used both to protect the instruments from dust contamination and external light and also to block scattered light generated from the optics. It's the same material used on the Quantum Noise Reduction system of Virgo for similar purposes [10].

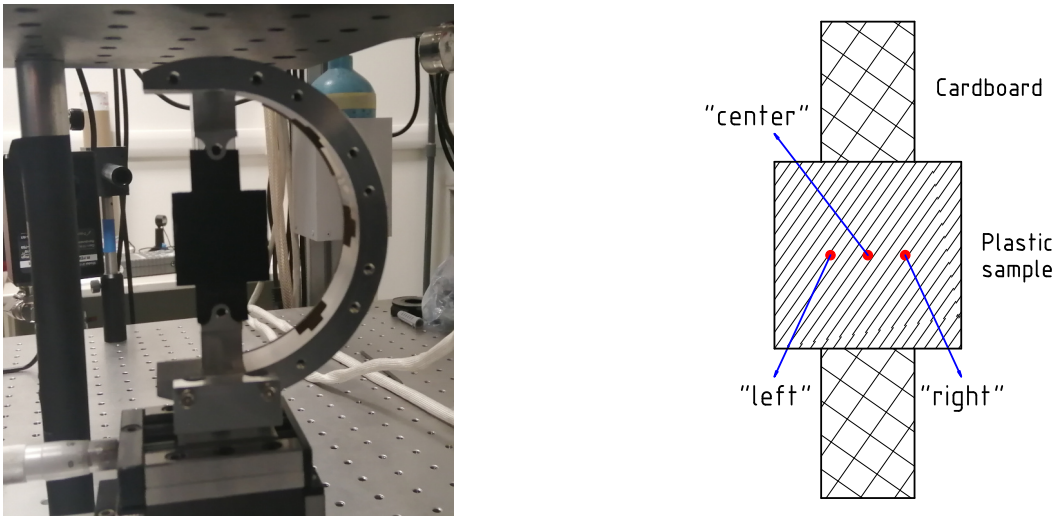

Figure 3.4: Left: plastic sample mounted on the scatterometer. Right: sketch of the plastic sample and label of the measured points.

The sample is a square of black plastic having side of 3 cm, thickness 5 mm and a low reflectivity. Since the available holder arms only admit samples thick at most 2 mm, this one couldn't be mounted directly. It was instead fixed to a piece of black cardboard, using tape, and this one was held by the arms (see figure 3.4). This is not an ideal solution as the tested surface is slightly forward with respect to the rotation center of the holder, but it's still a good compromise that allowed to take the measure regardless of the arms unsuitability. A consequence of this effect, however, is that the angle measured by the scatterometer (θ) isn't simply the sum of the incident and scattered angles (θ_i and θ_s). To compensate this a correction can be made using the formula obtained from the setup's geometry on figure 3.5 (left) and as explained in appendix A. The final result is equation (3.2) that considers the sample's displacement as its thickness (d=5 mm) and the radius of the main detector's circular trajectory around the sample h=345 mm.

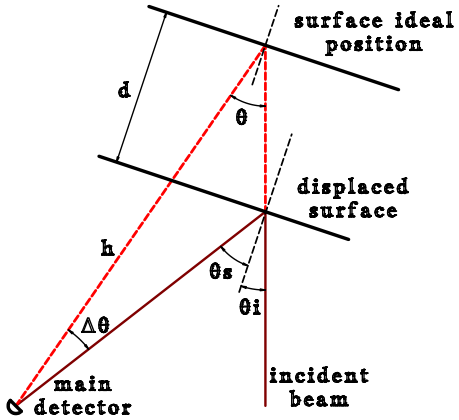

$$\theta_{corrected} = \theta_i + \theta_s = \theta + \Delta\theta = \approx \theta + \arcsin\left(\frac{\mathrm{d}\cdot\sin\theta}{\cos\theta_i\cdot\mathrm{h}}\right) \tag{3.2}$$

Figure 3.5: Left: outline of the plastic sample displacement. Right: angle measured by the scatterometer corrected by considering the surface displacement. Details on how the correction was found are reported in appendix A.

The material was found to show damages due to the high power intensity. In particular with a power of around 1 W and a beam radius $w \approx 0.5$ mm, the sample starts to produce smoke and visible damages after few seconds of exposure. At 0.5 W there are still visible damages, but no smoke, at least in the few seconds observed. This isn't a problem for the BSDF measure because, being its values fairly high, the usage of a low power beam, around the milliwatt, is required to not saturate the detector. No degradation was visibly observed in such condition.
Contrary to the silicon DSP, in this case no specular reflected beam was clearly visible due to the low reflectivity of the sample. This also explains why the dumper usually employed to block the specular reflected beam was found to have a negligible impact on the measures. The transmittance, measured using a power meter as for the silicon, was found to be compatible with zero.
Three spots on the sample, named as in figure 3.4 and distant 5 mm between themselves, were measured both with a filter ND1.3 for the reflected region and without it for the transmitted one. The results are reported in figure 3.6.

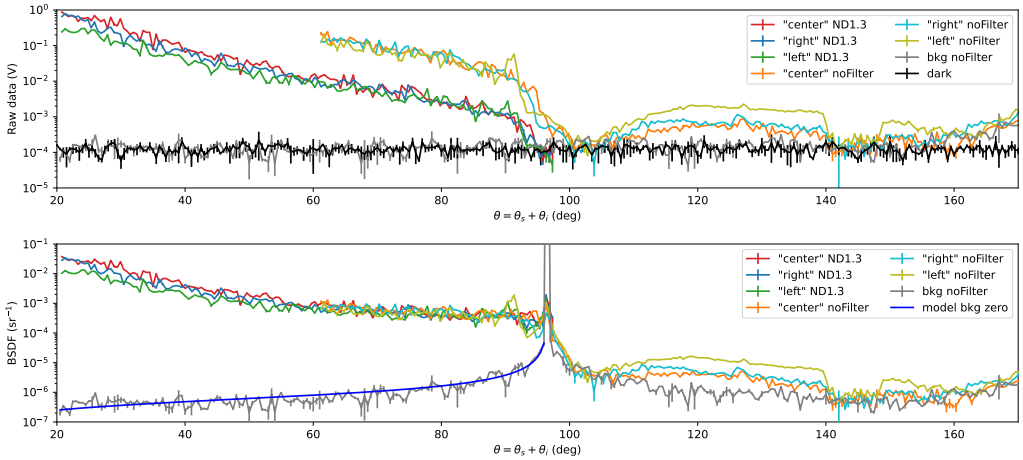

Figure 3.6: Plastic BSDF measures. Laser power ≈ 3.3 mW, incident angle $\theta_i = 6.5°$. For the first three measures, taken only for the reflection part, a filter *ND1.3* (table 3.1) was used in front of the main detector to not saturate it. This wasn't necessary for the other measures. The background model is from function (3.1) and its parameters values are reported in table 3.2. For all the measures, except *bkg* and *dark*, the angle θ was corrected using equation (3.2).

The background was taken under similar conditions to the other measures, but with the sample, including the cardboard piece, removed and without filter. For this reason it's also unnecessary to correct the associated angles. A preliminary fit on the background with equation 3.1 showed the parameter c to be compatible with zero, so the fit was repeated without this parameter ($c = 0$). The final results are reported in the second column of table 3.2. It can be noted that there is a significant difference between the plastic's background (figure 3.6) and the silicon's one (figure 3.2). Considering that the laser beam passes in the middle between the two arms, the reason for this difference can be found in the arms distance. As seen in figure 2.10, the farther apart the arms are, the lower the background tends to be. Therefore the fact that the plastic's background, having the two arms ≈ 7 cm distant from each other, is lower than the silicon's one for which the arms were ≈ 1.5 cm apart, is in agreement with what was discussed in section 2.3.
In the transmission part of figure 3.6, i.e. for $\theta > 96.5°$, a small signal can be seen without any filter on the detector. Around $\theta = 145°$ the typical shadow cast by the detector's support (figure 2.5) can be seen, so it can be assumed that this signal effectively originates from the laser's scattering. However, the use of a power meter was unsuccessful in detecting any power in the transmission zone, always giving a value comparable to the room's background (≈ 10 nW).
Note that between 60° and 96.5° both the measures taken with and without filter show approximately the same BSDF. This confirms that filter power reduction value in table 3.1 is correct.

Repeated measures on the same sample spot were also made to check their repeatability, both with and without the filter. The results are reported in figure 3.7.

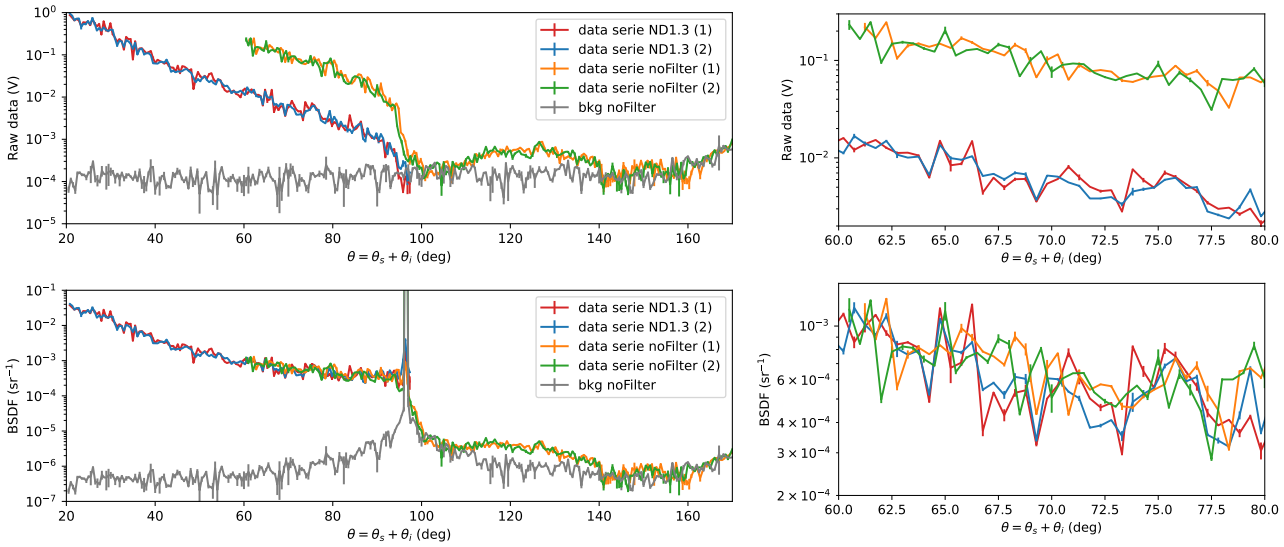

Figure 3.7: Repeated measure, on the same sample's spot, for the plastic (*left*). Same, but zoomed on the region 60°-80° (*right*). Laser's power $\approx 3.3\,\mathrm{mW}$, incident angle $\theta_i = 6.5°$.

The general trend of the data observed in figure 3.7 seems to be the same, but the variability between the different sets is higher than the one observed for the silicon DSP (figure 3.3 right), at least from a qualitative analysis. This particular behavior could be linked to the aforementioned sample instability to relative high laser power. However, to confirm this hypothesis, more tests are needed, such as comparing the variability of repeated measurements at various laser powers.

3.1.3 Black anodized aluminum profile

The sample is a black anodized aluminium profile with a length of 30 cm and a square base of side $\approx 4\,\mathrm{cm}$. Along with the plastic presented in the previous section, these profiles will be used in the new scatterometer's installation to realize the instrument's protective structure.

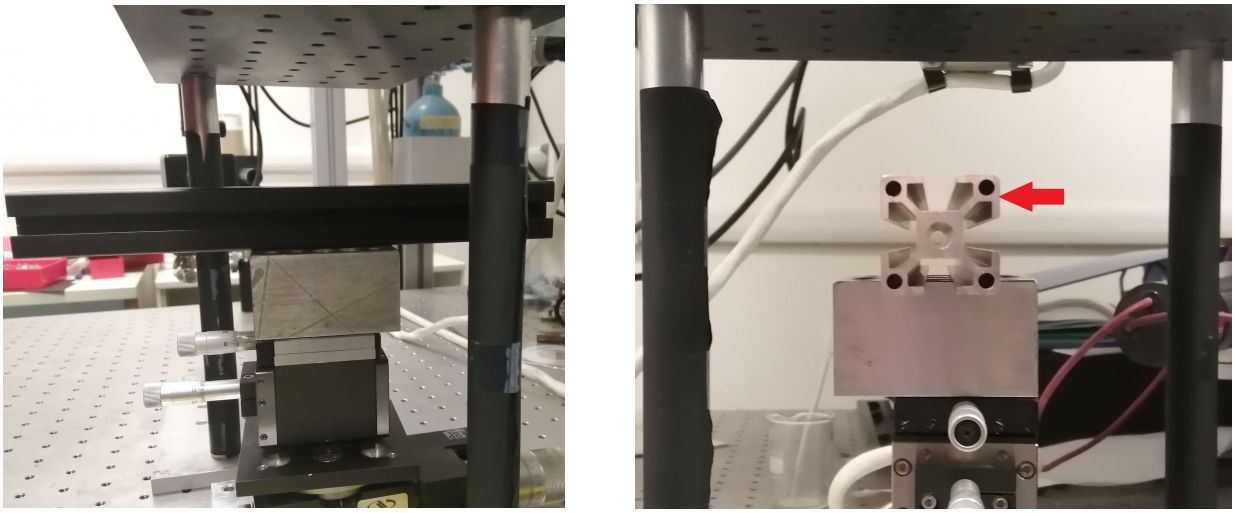

Figure 3.8: Surface of the aluminium sample facing towards the incident beam (*left*). Section of the aluminium sample (*right*). The beam's height was aligned to the external upper surface, indicated by the red arrow.

Given its dimensions, the standard sample holder cannot be used. So it was decided to simply place it on a metal finish aluminium block on the rotating platform, making sure that the surface facing towards the incident beam was aligned to the center of rotation. This situation is far from ideal because the various parts cannot be fixed to one another and are free to move. For this reason these measure are expected to not be very precise but useful just as coarse estimate of the BRDF of this

components.
The sample was found to be stable in all the power range of the laser, showing no visible damages or overheating. Regardless, a beam with a power of $\approx 4.5\,\mathrm{mW}$ and a filter ND1.3 (table 3.1) were used to not saturate the detector.
Three spots on the sample were measured: from 11 cm to 15 cm from the sample's left side, with a step size of 2 cm. The results are shown in figure 3.9.

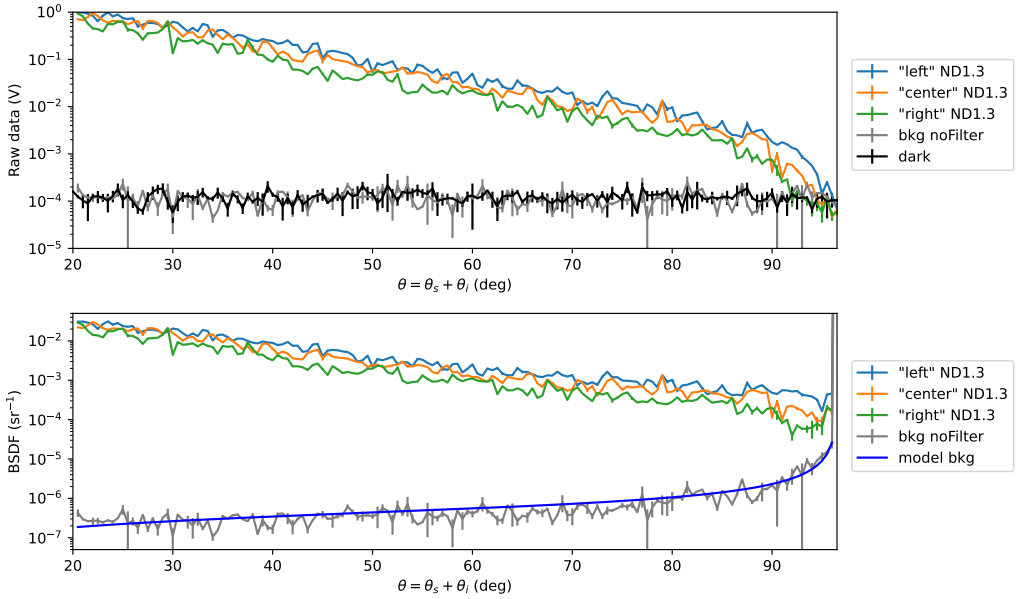

Figure 3.9: Aluminium BSDF measures. Laser power $\approx 4.5\,\mathrm{mW}$, incident angle $\theta_i \approx 6.5°$. The background model is from function (3.1) and its parameters values are reported in table 3.2

Only the part of the graph concerning the beam reflection ($\theta < 96.5°$) is reported because no significant transmitted light was detected. For the background, as for the plastic, a preliminary fit with function (3.1) showed the parameter c to be compatible with zero. So the fit was repeated without this parameter ($c = 0$) and the final results are reported in the third column of table 3.2. The overall trend of the aluminum's BSDF is similar to the plastic one, but their behaviors differ regarding the repeated measures. The aluminium ones are reported in figure 3.10.

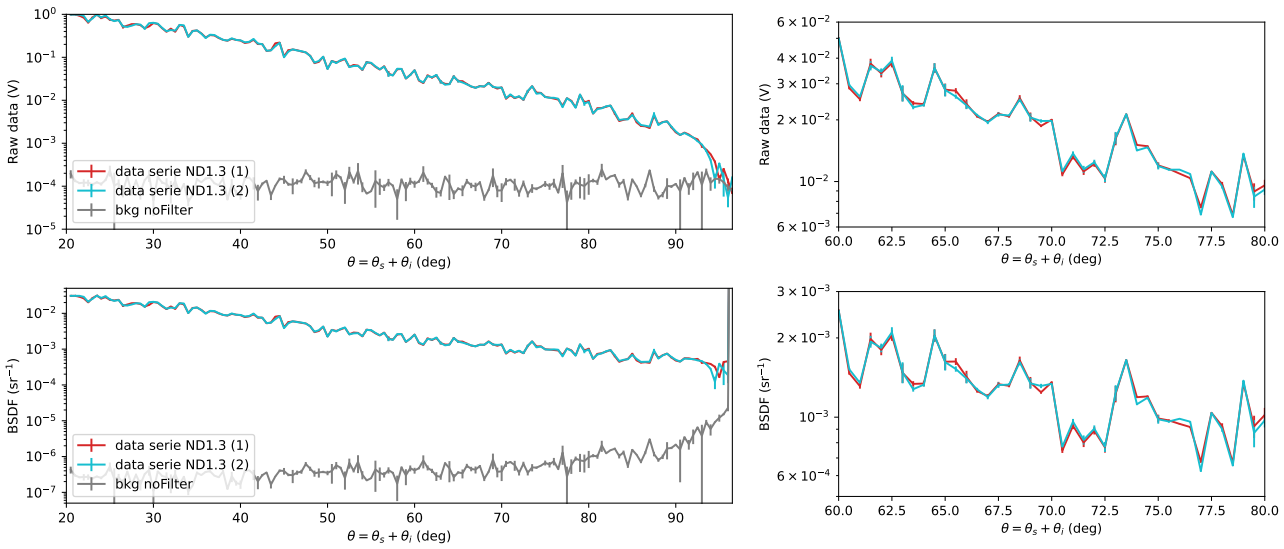

Figure 3.10: Repeated measure, on the same sample spot, for the anodized aluminium (*left*). Same, but zoomed on the region 60°-80° (*right*). Laser power $\approx 4.5\,\mathrm{mW}$, incident angle $\theta_i \approx 6.5°$.

The differences between the repeated measures are orders of magnitude smaller than the corresponding values, similar to what was observed for the *silicon DSP*.
Since a more rough surface tends to scatter more light and to give a higher BSDF [7], the fact that the BSDF value is generally higher for plastic and aluminium than for the polished silicon is in agreement with the literature, at least qualitatively.

	Silicon	Plastic	Aluminium
a $(\text{deg}^2\cdot\text{sr})^{-1}$	$(120 \pm 9) \cdot 10^{-8}$	$(-35 \pm 7) \cdot 10^{-8}$	$(-28 \pm 5) \cdot 10^{-8}$
b $(\text{deg}\cdot\text{sr})^{-1}$	$(-35 \pm 2) \cdot 10^{-7}$	$(8 \pm 1) \cdot 10^{-7}$	$(61 \pm 9) \cdot 10^{-8}$
c $(\text{sr})^{-1}$	$(28 \pm 2) \cdot 10^{-7}$	0	0

Table 3.2: Results of the background fits for the analyzed materials. The model used is reported in equation (3.1). For plastic and aluminium it was found the parameter "c" to be compatible with zero. So the fits were repeated without this parameter ($c = 0$).

3.2 Obtaining the TIS

The Total Integrated Scattering (TIS) is a parameter to characterize the overall scattering properties of materials. As reported in [7], the TIS can be defined as the ratio of scattered power in the reflected direction to the power incident on a surface. It can be expressed also as the integral of the BSDF over the projected solid angle of the hemisphere:

$$TIS = \int_{\Omega} BSDF(\theta_i, \phi_i, \theta_s, \phi_s) \cos\theta_s \, d\Omega \tag{3.3}$$

where $d\Omega = \sin(\theta_s) d\theta_s d\phi$.
To measure the TIS two main methods can be used. In the first one the BSDF, measured with a scatterometer, is fitted to a model (e.g., Harvey-Shack) and then equation (3.3) is used. However errors in the measured value of the BSDF and residuals between the model and the data can result in significant errors on the final TIS estimate. The second method, more reliable, is to directly measure the TIS using an integrating sphere [7] and it's the one that will be used in this thesis.

3.2.1 TIS measure with an integrating sphere

An integrating sphere is essentially a cavity internally covered with a white diffuse coating, with apertures (called ports) to allow for the beam to enter and exit, and the mounting of the samples and photodetectors. In particular the model used is the 4P4 of *Thorlabs* [11].

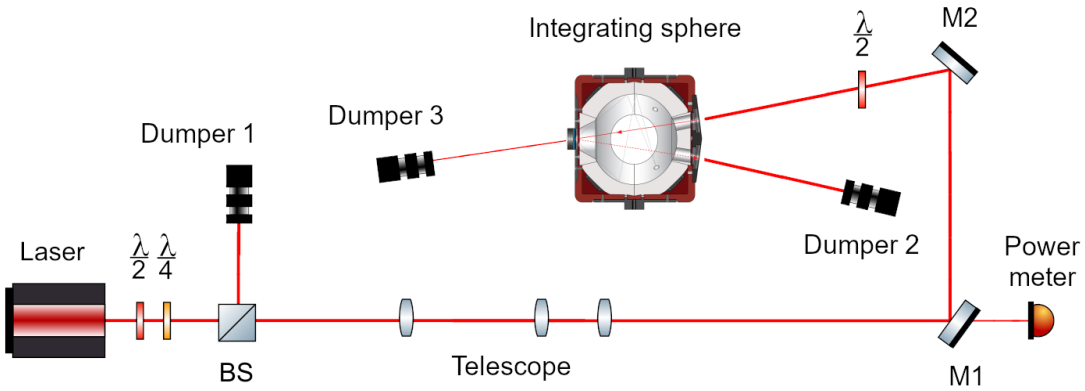

Figure 3.11: Optical layout of the integrating sphere. The size and separation of the elements are not on scale. Credit for the integrating sphere icon used: [11].

The setup diagram is reported in figure 3.11. A CW laser with a wavelength of 1064 nm and a beam radius of around ≈0.5 mm is used. The power (maximum is 1 W) can be regulated using a combination

of waveplates ($\lambda/2$ and $\lambda/4$) and beam splitter (BS). Two steering mirrors (*M1* and *M2*) are then used to direct the beam into the integrating sphere with an 8° angle from the surface's normal. A sample can be mounted on the port on the opposite side: the specular reflected beam is absorbed by *dumper 2*, while the transmitted one by *dumper 3*. Inside the sphere the scattered power is measured by a photodetector connected to its preamplifier (PDA) [12].

A power meter [13] was used to measure the residual power transmitted from the first steering mirror as a monitor of the power sent into the sphere. The latter can be obtained using the calibration line of figure 3.12. Its final value also needs to be corrected by the power meter offset which for taken measures was $P_{offs} = 25.7$ µW. This correction is already applied in all the data and results reported in this section.
The power's errors are obtained by considering a 3% maximum uncertainty on their values, as per power meter specifications, and a uniform probability distribution. Note that both errors on the x-axis and y-axis were taken into account for the fit.

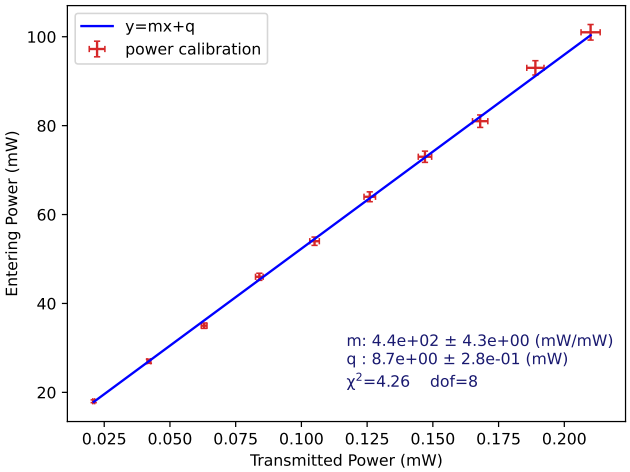

Figure 3.12: Calibration line: power entering the sphere vs power transmitted from the first steering mirror.

Before measuring the samples, the ambient light effect on the integrating sphere signal was tested. In reality it has no significant contribution on the final TIS value thanks to the followed procedure, but it's good practice to reduce possible interference. The following contributions were observed:

Measuring conditions	PDA current (nA)
All lights off	0
All lights on	21
Working condition	0.3

Table 3.3: Effect of ambient light on the integrating sphere signal.

A reference line was obtained by measuring the scattered light from a diffusive cap made of the same inner material of the integrating sphere. To do this the cap was first mounted on the appropriated sphere's port. Ten measures of entering power and PDA current were taken and are reported in figure 3.13.

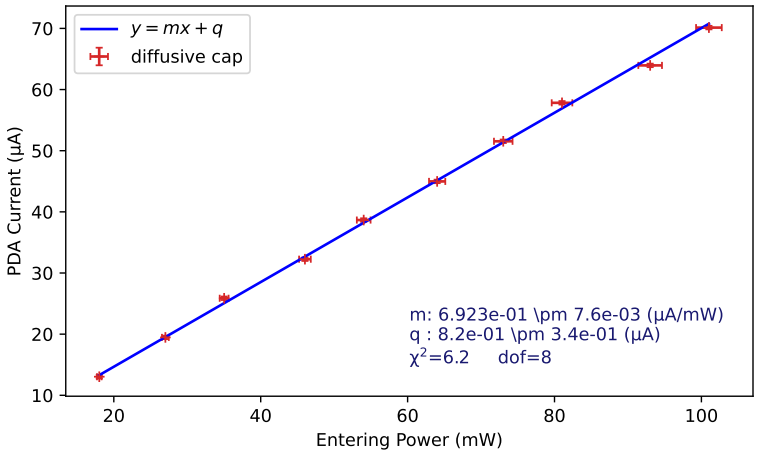

Figure 3.13: Reference line for TIS measures: PDA signal at different powers for the diffusive cap.

For the errors on the current it was considered a maximum 0.05% uncertainty on the values, as per PDA specifications [12], and a uniform probability distribution. Like before both errors on the x and y axis were considered in the fit. The χ^2 value is smaller than the degree of freedom (dof), so the hypothesis that the data follows a linear trend can surely be accepted with a 95% confidence level.
From this type of fit, the most relevant parameter obtained is the slope (m). In an integrating sphere the TIS can be computed as the ratio between the power scattered from the sample and from the diffusive cap [14]. This can be generalized by taking, instead of the powers, the slopes (m) of proportionality between PDA current and sphere's entering power, as obtained before. The advantages are that constant backgrounds, like the environment light, don't contribute to the TIS and it's also not necessary to calibrate the PDA.
Various corrections to this quantity may be considered, such as the fraction of power escaping the sphere and the one collected by the photodiode. In first approximation these corrections can be considered negligible [14]. Instead, the slope values were corrected by removing the ambient scattering contribution, $m_\infty = (59 \pm 5)10^{-6}$ µA/mW, a parameter that was established by other members of the Virgo group of Padova [15]. So, considering m_{ref} the slope found for the reference line in figure 3.13 and m_{sample} the analogous quantity, but referred to the specific sample in exam instead of the diffusive cap, the TIS can be computed as in equation 3.4 and the associated error from the propagation of uncertainty.

$$TIS = \frac{m_s - m_\infty}{m_{ref} - m_\infty} \tag{3.4}$$

Samples were analyzed in a similar way as the diffusive cap. The obtained results are reported below.

For the *silicon DSP* both surfaces of the sample, labelled *sideA* and *sideB*, were analyzed. Three different points were taken on the former, one on the latter. The measures are displayed in figure 3.14 while the fits results in table 3.4.

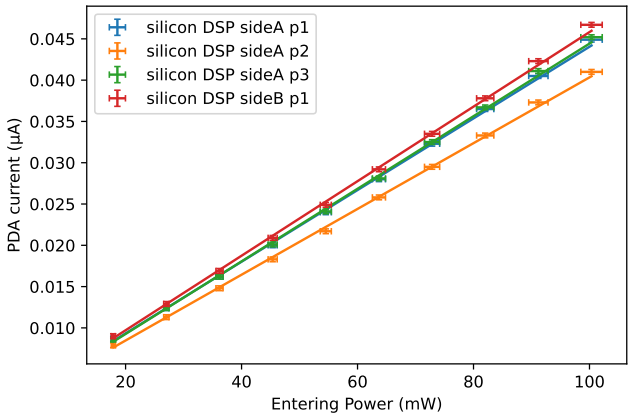

Figure 3.14: Silicon DSP sample measures with the integrating sphere.

	sideA p1	sideA p2	sideA p3	sideB p1
m (µA/mW)	$(434 \pm 4)10^{-6}$	$(398 \pm 4)10^{-6}$	$(440 \pm 4)10^{-6}$	$(451 \pm 4)10^{-6}$
q (µA)	$(7 \pm 2)10^{-4}$	$(5 \pm 2)10^{-4}$	$(5 \pm 2)10^{-4}$	$(7 \pm 2)10^{-4}$
χ^2	3.2	3.4	3.3	2.8
dof	8	8	8	8
TIS	$(54 \pm 1)10^{-5}$	$(49 \pm 1)10^{-5}$	$(55 \pm 1)10^{-5}$	$(57 \pm 1)10^{-5}$

Table 3.4: Results of the linear fit ($y = mx + q$) on the silicon DSP sample measured with the integrating sphere. The displayed χ^2 values are the referred to the total χ^2, not the reduced one.

For the *plastic* sample two measures were taken, one for each side, labelled *sideA* and *sideB* (figure 3.15). During the measurements *sideA* was visibly dirty (residue of tape's glue) and may not give

accurate results, while *sideB* was cleaner. The signal (PDA current) at around 100 mW was observed to be unstable (drifting towards lower current values). For this reason I used the data up to 80 mW. This may be linked to the sample laser damage threshold already discussed in section 3.1.2.

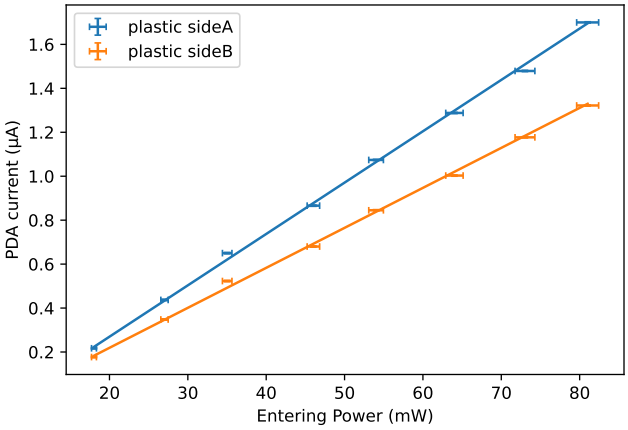

	Pl. sideA	Pl. sideB
m (µA/mW)	$(234 \pm 3)10^{-4}$	$(182 \pm 3)10^{-4}$
q (µA)	$(-20 \pm 1)10^{-2}$	$(-14 \pm 1)10^{-2}$
χ^2	6.6	9.9
dof	6	6
TIS	$(337 \pm 6)10^{-4}$	$(262 \pm 5)10^{-4}$

Figure 3.15: Left: plastic sample measures with the integrating sphere. Right: results of the linear fits. The displayed χ^2 values are the referred to the total χ^2, not the reduced one.

The *anodized aluminium* sample doesn't have a large plane surface, so it wasn't possible to completely cover the sphere's aperture port. This means that the results may not be very representative for the specific material, as there may be a loss of scattered light from the uncovered part of the port. Two points on the sample were measured, similarly to section 3.1.3, distant around 2 cm from one another. Results are in figure 3.16.

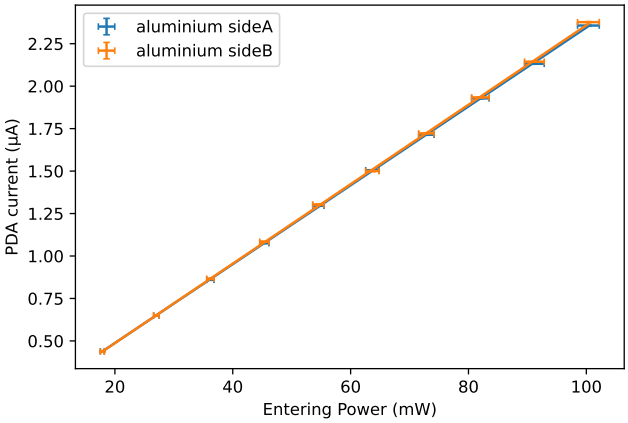

	Al. p1	Al. p2
m (µA/mW)	$(2322 \pm 5)10^{-5}$	$(2339 \pm 6)10^{-5}$
q (µA)	$(23 \pm 2)10^{-3}$	$(19 \pm 2)10^{-3}$
χ^2	0.2	0.4
dof	8	8
TIS	$(335 \pm 4)10^{-4}$	$(337 \pm 4)10^{-4}$

Figure 3.16: Left: anodized aluminium sample measures with the integrating sphere. Right: results of the linear. The displayed χ^2 values are the referred to the total χ^2, not the reduced one.

The fits of all the three materials have a $\chi^{(2)}$ value smaller or similar to the degree of freedoms, so the linearity hypothesis isn't rejectable with a 95% confidence level. The two measurements of TIS for the plastic samples are not compatible with each other within their errors. A possible explanation for this incompatibility may be found in the different cleanliness conditions of the two sides. Similarly some silicon's results aren't compatible within their errors, but this may be explained by the already discussed conditions of the sample which may also have caused differences in the BSDF trends seen in figure 3.3. Instead the aluminium results are very similar to each other and, given their errors, in a good compatibility. It's also worth pointing out that, regardless of the errors, the TIS values found for the plastic and aluminium samples are similar to each other, as it was expected given that their BSDF trends (figures 3.6 and 3.9) are also similar, and higher than the polished silicon (again expected because the latter's BSDF is generally lower).

Chapter 4

Conclusion

In this thesis I characterized the scatterometer's setup of the Virgo group of Padova. The work done made it possible to find out that the sample holder arms give a significant contribution to the general background level. The introduction of an additional iris in the layout has reduced this background, even if partially.
Light scattering properties of materials relevant for the Virgo group of Padova were characterized both in terms of angular dependency through the BSDF and overall using the TIS. This was done to test the measuring procedures on real samples and also because the plastic material and the aluminium profiles will be used in a new installation of the scatterometer, so it is useful to know their properties. In the new installation the scatterometer will be located in a clean room in order to reduce the effects of dust particles on the measures. The setup will include the integrating sphere in the optical setup so that the BSDF and TIS measures may be taken in an easier way. Other wavelengths will also be available to test and a system to change the beam radius on the sample will be implemented. Furthermore the minimum angular distance from the specular reflected beam at which the BSDF measures can be taken will be reduced, thus allowing for better characterizations of the samples.

Appendix A

Correction of a displaced sample for BSDF measures with the scatterometer

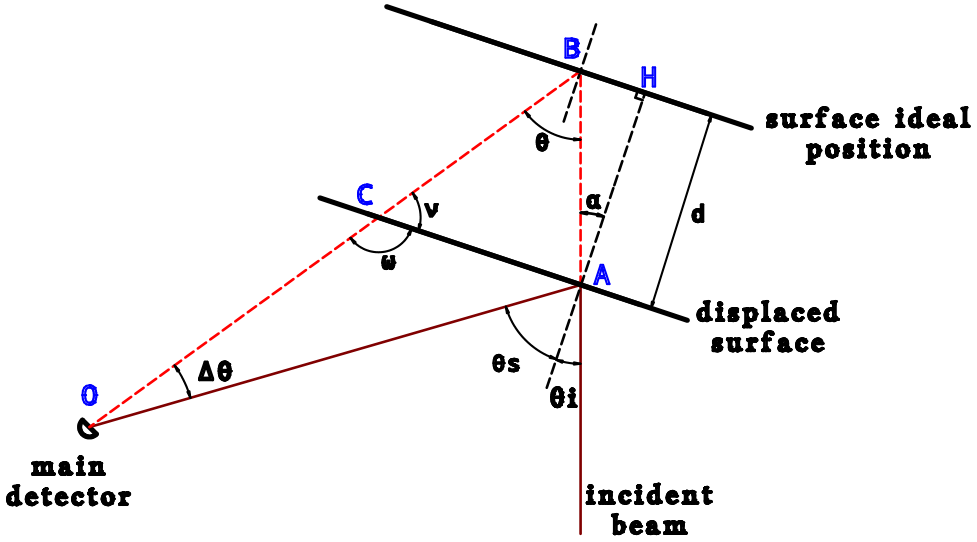

Figure A.1: Diagram a sample displaced with respect to the scatterometer's center

Referring to figure A.1, consider the ideal situation in which the laser beam encounter the sample's surface in the point "B", which corresponds to the *center of rotation* of the main detector that measures the scattered light in "O". In this ideal scenario the measured angle "θ" is the sum of the incident angle θ_i and the scattered one θ_s, as represented in figure 1.1 (right). $\theta_i + \theta_s$ is, in fact, the quantity that's relevant to measure, but when the sample's surface is displaced forward of "d" it can be seen that $\theta_{corrected} = \theta_i + \theta_s = \theta + \Delta\theta$. Therefore it's necessary to compute the correction $\Delta\theta$. From the law of sines applied to the triangle ΔOAC:

$$\sin(\Delta\theta) = \overline{AC}/\overline{OA} \cdot \sin(\omega) \tag{A.1}$$

To compute $\overline{AC}$ in eq. (A.1), first it can be considered the right triangle ΔAHB. Having $\overline{AH} = d$ the sample surface displacement and $\alpha = \theta_i$ the beam incident angle, the segment $\overline{AB}$ can be found:

$$\overline{AB} = \frac{\overline{AH}}{\cos(\alpha)} = \frac{d}{\cos(\theta_i)} \tag{A.2}$$

$\overline{AC}$ is given by the law of sines applied to ΔABC and equation (A.2):

$$\overline{AC} = \overline{AB} \cdot \frac{\sin\theta}{\sin\nu} = \frac{d}{\cos(\theta_i)} \cdot \frac{\sin\theta}{\sin\nu} \tag{A.3}$$

The segment $\overline{OA}$ in eq. (A.1) could be found by applying the law of cosines to the triangle ΔOAB, with $\overline{OB} = h = 345\,\text{mm}$ the radius of the main detector's circular trajectory around the sample. However, since the sample displacement $d = 0.5\,\text{mm} << h$ and $\theta_i = 6.5°$ is relatively small, the segment $\overline{OA}$ can be approximated with h:

$$\overline{OA} = \sqrt{\overline{OB}^2 + \overline{AB}^2 - 2\,\overline{OB}\,\overline{AB}\,\cos(\theta)} = \sqrt{h^2 + \frac{d^2}{\cos(\theta_i)^2} - \frac{2hd\cos(\theta)}{\cos(\theta_i)}} \approx h \tag{A.4}$$

Finally, considering $\omega = \pi - \nu$ and substituting equations (A.3) and (A.4) in (A.1), $\Delta\theta$ can be obtained:

$$\sin(\Delta\theta) \approx \frac{d}{\cos(\theta_i)} \cdot \frac{\sin\theta}{\cancel{\sin\nu}} \cdot \frac{1}{h} \cdot \cancel{\sin(\pi - \nu)}$$

$$\Delta\theta \approx \arcsin\left(\frac{d \cdot \sin(\theta)}{\cos(\theta_i) \cdot h}\right) \tag{A.5}$$

Equation (A.5) is used in section 3.1.2 to correct the angles of the BSDF measures for the plastic sample. Note that since the BSDF depends from the angle θ_s (equation 2.1) and this can be found as $\theta_s = \theta_{corrected} - \theta_i = \theta + \Delta\theta - \theta_i$, then the correction (A.5) also slightly affects the BSDF values themselves.

Bibliography

[1] Virgo Collaboration. Detector. [Online]. Available: https://www.virgo-gw.eu/science/detector/

[2] LIGO Laboratory. Ligo - a gravitational-wave interferometer. [Online]. Available: https://www.ligo.caltech.edu/page/ligo-gw-interferometer

[3] Virgo Collaboration. Astrophysical sources of gravitational waves. [Online]. Available: https://www.virgo-gw.eu/science/gw-universe/astrophysical-sources-of-gw/

[4] The LIGO Scientific Collaboration and the Virgo Collaboration and the KAGRA Collaboration, "GWTC-3: Compact binary coalescences observed by ligo and virgo during the second part of the third observing run," 2021.

[5] LIGO Scientific Collaboration and Virgo Collaboration, "GWTC-1: A gravitational-wave transient catalog of compact binary mergers observed by LIGO and virgo during the first and second observing runs," *Physical Review X*, vol. 9, no. 3, sep 2019. [Online]. Available: https://doi.org/10.1103%2Fphysrevx.9.031040

[6] Virgo Collaboration. Sensitivity. [Online]. Available: https://www.virgo-gw.eu/science/detector/sensitivity/

[7] E. Fest, *Stray Light Analysis and Control*. SPIE, 2013, vol. PM229.

[8] E. Polini, R. Bonnand, M. D. Laurentis, and E. Tournefier, "Note on optimal aperture radius for diaphragms and baffles," *Virgo TDS*, Oct 2020. [Online]. Available: https://tds.virgo-gw.eu/ql/?c=15957

[9] A. Moscatello, "Light scattering from dust contamination in gravitational-wave interferometric detectors," Master's thesis, Università degli Studi di Padova, 2022.

[10] L. Conti, private communication.

[11] Thorlabs. [Online]. Available: https://www.thorlabs.com/thorproduct.cfm?partnumber=4P4

[12] ——. [Online]. Available: https://www.thorlabs.com/thorproduct.cfm?partnumber=PDA200C

[13] ——. [Online]. Available: https://www.thorlabs.com/thorproduct.cfm?partnumber=PM160

[14] B. D'Angelo, "Numerical simulations of stray light in virgo," Ph.D. dissertation, Università degli Studi di Genova, 2022. [Online]. Available: https://hdl.handle.net/11567/1086404

[15] Padova group, "Report on TIS and BSDF of four samples of AdV-Ph2 baffles," *private communication*, 2023.